

# Generative Neural Operators through Diffusion Last Layer

Sungwon Park<sup>1,2</sup> Anthony Zhou<sup>2</sup> Hongjoong Kim<sup>1</sup> Amir Barati Farimani<sup>2</sup>

## Abstract

Neural operators have emerged as a powerful paradigm for learning discretization-invariant function-to-function mappings in scientific computing. However, many practical systems are inherently stochastic, making principled uncertainty quantification essential for reliable deployment. To address this, we introduce a simple add-on, the *diffusion last layer* (DLL), a lightweight probabilistic head that can be attached to arbitrary neural operator backbones to model predictive uncertainty. Motivated by the relative smoothness and low-dimensional structure often exhibited by PDE solution distributions, DLL parameterizes the conditional output distribution directly in function space through a low-rank Karhunen-Loëve expansion, enabling efficient and expressive uncertainty modeling. Across stochastic PDE operator learning benchmarks, DLL improves generalization and uncertainty-aware prediction. Moreover, even in deterministic long-horizon rollout settings, DLL enhances rollout stability and provides meaningful estimates of epistemic uncertainty for backbone neural operators.

## 1. Introduction

To approximate function-to-function mappings with neural surrogates, neural operators have emerged as a general paradigm and have been studied extensively across diverse architectures (Kovachki et al., 2023; Azizzadenesheli et al., 2024). Representative approaches include DeepONet, which parameterizes operators via a branch-trunk decomposition (Lu et al., 2021), and the Fourier neural operator (FNO), which employs global spectral convolutions to enable discretization-robust learning (Li et al., 2020). Subsequent work has expanded this line of research through improved scalability (Tran et al., 2023), extensions to geo-

<sup>1</sup>Korea University, Seoul, South Korea <sup>2</sup>Carnegie Mellon University, Pittsburgh, USA. Correspondence to: Hongjoong Kim <hongjoong@korea.ac.kr>, Amir Barati Farimani <barati@cmu.edu>.

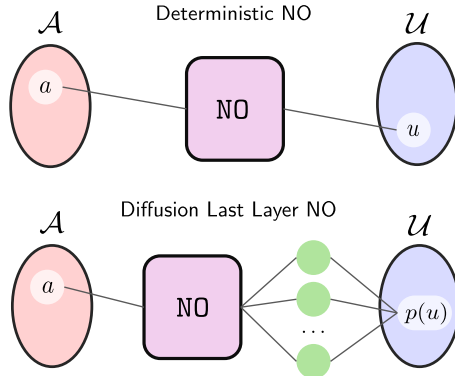


Figure 1. Deterministic vs. generative neural operators. A standard neural operator (top) maps an input field  $a \in \mathcal{A}$  to a single prediction  $u \in \mathcal{U}$ . Our *Diffusion Last Layer* (bottom) turns the same backbone into a conditional generator by attaching a lightweight diffusion head, producing a full predictive distribution  $p(u | a)$  over functions rather than a point estimate.

metric and irregular domains (Li et al., 2023a;b), spherical and multiscale encoder-decoder operator designs (Bonev et al., 2023; Rahman et al., 2023), and attention-based operator models that better capture long-range dependencies in complex PDE systems (Li et al., 2023c; Hao et al., 2023; 2024; Herde et al., 2024).

In many scientific applications, the target field exhibits intrinsic randomness arising from stochastic forcing, unresolved subgrid-scale effects, uncertain coefficients, or chaotic sensitivity, making accurate uncertainty quantification (UQ) essential for reliable surrogate modeling (Xiu, 2010). Motivated by this need, recent advances in scientific machine learning have developed probabilistic operator learning frameworks that model conditional distributions over functions, rather than returning deterministic point predictions (Psaros et al., 2023). Representative approaches include Bayesian neural operators (Lin et al., 2023; Weber et al., 2024; Magnani et al., 2025a;b), which aim to capture epistemic uncertainty via posterior inference over model parameters. Complementary lines of work instead construct generative operator surrogates that directly sample diverse realizations from the conditional solution distribution (Bülte et al., 2025), or train function space generative models using neural operator parameterizations (Rahman et al., 2022; Shi

et al., 2025).

Meanwhile, recent progress in diffusion models (Sohl-Dickstein et al., 2015; Ho et al., 2020; Song et al., 2021) and flow matching (Liu et al., 2023; Lipman et al., 2023) for high-dimensional fields has provided a new route to probabilistic PDE surrogates. These generative frameworks have been actively explored in scientific forecasting and data assimilation, particularly under sparse or partial observations (Lippe et al., 2023; Shysheya et al., 2024; Huang et al., 2024). To improve scalability, latent generative formulations compress the solution state space while largely preserving predictive fidelity (Rozet et al., 2025; Zhou et al., 2025b). Related encoder-based designs further extend these models to irregular domains and geometric settings, enabling conditional generation beyond regular grids (Zhou et al., 2025a; Wang et al., 2025).

In this work, we propose the diffusion last layer (DLL), a simple add-on that converts any deterministic neural operator backbone into a generative surrogate for random field prediction and uncertainty quantification, shown in Figure 1. DLL is architecture agnostic: it preserves the backbone’s discretization invariance and geometry handling while enabling expressive conditional sampling. Furthermore, to make diffusion sampling efficient at high resolutions, the diffusion head is trained over a latent coefficient space produced by an operator encoder rather than in pixel space, substantially reducing cost without sacrificing fidelity. Across stochastic operator learning benchmarks, DLL yields more accurate predictions and better-calibrated uncertainty, and it also improves stability in long-horizon rollouts.

## 2. Background

### 2.1. Operator Learning

Many scientific relationships, especially in physical simulation, can be formulated as *operators*:

$$\mathcal{G}^\dagger : \mathcal{A} \rightarrow \mathcal{U},$$

where  $\mathcal{A}$  and  $\mathcal{U}$  are function spaces and the output is determined by a deterministic rule (Kovachki et al., 2023; Azizzadenesheli et al., 2024).

For stochastic systems, it is natural to generalize deterministic operators to *stochastic operators*:

$$\mathcal{G}^\ddagger : \mathcal{A} \rightarrow \mathcal{R}(\mathcal{U}),$$

where  $\mathcal{R}(\mathcal{U})$  denotes the space of  $\mathcal{U}$ -valued random functions. Equivalently,  $\mathcal{G}^\ddagger(a)$  specifies a conditional distribution over outputs  $u \mid a$ , so that a single input function induces a distribution of possible solutions rather than a unique realization (Bülte et al., 2025).

Deterministic operators are recovered as a special case: if

$\mathcal{G}^\ddagger(a) = \delta_{\mathcal{G}^\dagger(a)}$ , then the conditional law collapses to a Dirac measure concentrated at  $\mathcal{G}^\dagger(a)$ .

We adopt a unified probabilistic formulation of operator learning. Given a dataset

$$\mathcal{D} = \{(a^{(i)}, u^{(i)})\}_{i=1}^N, \quad u^{(i)} \sim \mathcal{G}^\ddagger(a^{(i)}), \quad (1)$$

the goal is to learn a parameterized operator  $\mathcal{G}_\theta$  that approximates the ground-truth mapping. Depending on whether the conditional distribution  $\mathcal{G}^\ddagger(a)$  is degenerate or genuinely stochastic, we distinguish two regimes of operator learning.

**Problem 2.1** (Stochastic Problem). Given the dataset  $\mathcal{D}$  in (1), the goal is to learn an approximation of the ground-truth stochastic operator  $\mathcal{G}_\theta \stackrel{d}{\approx} \mathcal{G}^\ddagger$ .

This setting arises in stochastic dynamical systems with random forcing, unresolved microscale physics, and other regimes where output variability is intrinsic. Such stochasticity naturally appears in SPDE learning (Salvi et al., 2022; Chen et al., 2024) and in weather forecasting, where probabilistic prediction and ensemble uncertainty quantification are essential (Pathak et al., 2022; Price et al., 2025).

**Problem 2.2** (Deterministic Problem). Given the same dataset  $\mathcal{D}$  in (1), there is a ground-truth deterministic operator  $\mathcal{G}^\dagger$ , and the data are collected without randomness:

$$u^{(i)} = \mathcal{G}^\dagger(a^{(i)}) \quad \forall i.$$

The goal is to learn an approximation  $\mathcal{G}_\theta \approx \mathcal{G}^\dagger$ .

This setting arises in surrogate modeling for deterministic physical systems, where one learns a fast approximation of a high-fidelity PDE solver mapping inputs to solution fields. Such surrogates enable rapid parameter sweeps, inverse problems, and design optimization (Kovachki et al., 2023; Azizzadenesheli et al., 2024). Even in this deterministic setting, uncertainty quantification is often desired by modeling a distribution over outputs to capture epistemic uncertainty from limited data or model misspecification.

Finally, although these problem classes are often treated with different model families, we take a unified viewpoint: conditional diffusion models provide a single, flexible framework that can represent both deterministic operators and intrinsically stochastic operators, while also enabling principled uncertainty quantification when desired.

### 2.2. Conditional Diffusion Models

In this subsection, we review conditional diffusion models from the perspective of operator learning, with the goal of modeling distributions over solution fields in stochastic operator learning. While several recent works formulate diffusion processes directly in infinite-dimensional function spaces (Lim et al., 2023; Kerrigan et al., 2023; 2024; Lim

et al., 2025; Shi et al., 2025), our DLL framework instead operates on a compact finite-dimensional coefficient representation.

We slightly abuse notation and write the dataset as condition target pairs

$$\mathcal{D} = \{(c^{(i)}, x^{(i)})\}_{i=1}^N \quad (2)$$

interchangeably with (1) for notational convenience. In (2), we assume the target output admits a finite-dimensional representation  $x \in \mathbb{R}^{d_x}$  (e.g., latent variables or low-rank coefficient vectors).

We begin by recalling that diffusion models and flow-matching models can be viewed under a unified generative framework (Lai et al., 2025; Gao et al., 2025). Throughout this paper, we refer to this unified family simply as *diffusion models*. The objective is the standard conditional generative modeling problem of learning the conditional law  $p(x | c)$ .

To this end, diffusion models construct a denoising mechanism that transports a simple noise distribution  $p_{\text{noise}}$  to the target conditional distribution  $p(\cdot | c)$ . We introduce the forward noising process

$$x_t = a_t x + b_t \epsilon, \quad 0 \leq t \leq T, \quad (3)$$

where  $\epsilon \sim p_{\text{noise}}$  and  $a_t, b_t$  are differentiable scheduling functions chosen such that  $x_t$  gradually approaches pure noise as  $t \rightarrow T$ .

Given (3), the goal is to learn a reverse-time dynamics that enables sampling from  $p(x | c)$ . Among several equivalent parameterizations, we focus on the *flow-based* formulation via *velocity prediction* for clarity (Lipman et al., 2023; Liu et al., 2023). In this framework, there exists a velocity field  $v(\cdot, t, c)$  such that the conditional densities  $\rho_t(\cdot | c) = p(x_t | c)$  satisfy the continuity equation

$$\partial_t \rho_t + \nabla \cdot (\rho_t v) = 0, \quad \rho_T(\cdot | c) = p_{\text{noise}}(\cdot).$$

Sampling is then performed by integrating the probability flow ODE backward in time:

$$dx_t = v(x_t, t, c) dt, \quad x_T \sim p_{\text{noise}}.$$

The remaining task is to learn the velocity field from data. For the linear noising process (3), the *oracle* velocity along the coupling  $(x, \epsilon)$  is given by

$$v^*(x_t, t, c) = \dot{a}_t x + \dot{b}_t \epsilon.$$

Accordingly, we train a neural velocity field  $v_\phi$  by minimizing the conditional velocity-matching objective

$$\mathcal{L}_V(c) = \mathbb{E}_{x,t} \left[ \|v_\phi(x_t, t, c) - (\dot{a}_t x + \dot{b}_t \epsilon)\|_2^2 \right]. \quad (4)$$

To compare stochastic and deterministic conditional targets in a unified way, we measure distributional error using the 2-Wasserstein distance between the learned distribution  $\rho_0(\cdot | c)$  and the target  $p(\cdot | c)$ . Prior work shows that score-based diffusion training admits a Wasserstein distance minimization interpretation (Kwon et al., 2022). In a similar vein, we can show that small velocity matching error implies small transport error.

**Proposition 2.3.** *Fix  $c$ . Under suitable regularity conditions, there exists a constant  $C > 0$  such that*

$$\mathcal{W}_2(p(\cdot | c), \rho_0(\cdot | c)) \leq C \sqrt{\mathcal{L}_V(c)}.$$

The above proposition follows from stability estimates for the continuity equation with respect to perturbations of the velocity field. Since the Wasserstein distance naturally accommodates both absolutely continuous distributions and singular measures such as Dirac deltas, Proposition 2.3 implies that diffusion models can approximate solutions to both Problems 2.1 and 2.2 by minimizing the objective  $\mathcal{L}_V$ . A proof and further discussion are provided in Appendix A.1.

It is also worth noting that (4) is minimized over the empirical dataset (2), rather than the full population distribution. Nevertheless, recent theoretical and empirical studies suggest that diffusion models can generalize beyond the training samples despite not driving the training loss to zero (Kadkhodaie et al., 2024; Bonnaire et al., 2025; Song et al., 2025). In practice, diffusion models often exhibit *underfitting* of (4), which can improve generalization. We discuss this phenomenon further in the next section.

### 3. Uncertainty Quantification and Probabilistic Surrogates

In this section, we examine how *conditional diffusion models* can serve as probabilistic surrogates for the operator learning tasks formulated in Problems 2.1 and 2.2. We begin by discussing uncertainty quantification and probabilistic modeling in these settings, and then show how conditional diffusion models provide a unified framework for addressing both problems.

#### 3.1. Uncertainty Quantification

We study the problem of learning a *probabilistic surrogate*  $\mathcal{G}_\theta$  that approximates the ground-truth stochastic operator  $\mathcal{G}^\dagger$ . Here  $\theta$  denotes the learnable quantity determined by the model class and training algorithm (e.g., neural network parameters; see Table 1). Depending on the formulation,  $\theta$  may represent a point estimate or a distribution over parameters. Since operator learning is typically ill-posed and data are finite, some approximation error is unavoidable. For a fixed input  $a$ , the total distributional error admits the

*Table 1.* Model comparison across uncertainty representations. Deterministic surrogates (NN) learn a point estimate of parameters, Bayesian models (BNN) infer a posterior to capture epistemic uncertainty, and diffusion-based surrogates (DM, LDM, DLL) learn conditional generative models that approximate the conditional output distribution  $\mathcal{G}^\dagger(a)$ .

Methods	$\theta$	Estimates	$\mathcal{G}_\theta(a)$
NN	NN Param	$\theta \mid \mathcal{D}$	$\approx \mathcal{G}^\dagger(a)$
BNN	NN Param	$p(\theta \mid \mathcal{D})$	$\overset{p}{\approx} \mathcal{G}^\dagger(a)$
DM	Data Vector	$p(\theta \mid \mathcal{D}, a)$	$\overset{d}{\approx} \mathcal{G}^\dagger(a)$
LDM	Latent Vector	$p(\theta \mid \mathcal{D}, a)$	$\overset{d}{\approx} \mathcal{G}^\dagger(a)$
DLL	LL Param	$p(\theta \mid \mathcal{D}, a)$	$\overset{d}{\approx} \mathcal{G}^\dagger(a)$

decomposition

$$\underbrace{\mathcal{W}_2(\mathcal{G}^\dagger(a), \mathcal{G}_\theta(a))}_{\text{total error}} \leq \underbrace{\mathcal{W}_2(\mathcal{G}^\dagger(a), \mathcal{G}_{\theta^*}(a))}_{\text{model misspecification}} + \underbrace{\mathcal{W}_2(\mathcal{G}_{\theta^*}(a), \mathcal{G}_\theta(a))}_{\text{epistemic uncertainty}},$$

where  $\theta^*$  is an oracle estimator induced by the hypothesis class and optimization procedure. The model misspecification term reflects the intrinsic limitation of the chosen surrogate family, while the epistemic uncertainty term arises from finite data and typically decreases as the dataset grows. In addition,  $\mathcal{G}^\dagger$  may exhibit *aleatoric uncertainty*, i.e., irreducible randomness in the conditional output distribution.

As a special case, consider learning a *deterministic surrogate*  $\mathcal{G}_\theta \approx \mathcal{G}^\dagger$  in Problem 2.2. If the observed output is subject to stochastic variability around the deterministic solution, the pointwise prediction error can be decomposed as  $u \sim \mathcal{G}^\dagger(a)$ , the error admits a more explicit decomposition:

$$\underbrace{\|u - \mathcal{G}_\theta(a)\|}_{\text{total error}} \leq \underbrace{\|u - \mathcal{G}^\dagger(a)\|}_{\text{aleatoric uncertainty}} + \underbrace{\|\mathcal{G}^\dagger(a) - \mathcal{G}_{\theta^*}(a)\|}_{\text{model misspecification}} + \underbrace{\|\mathcal{G}_{\theta^*}(a) - \mathcal{G}_\theta(a)\|}_{\text{epistemic uncertainty}}.$$

The goal of UQ is to capture both *aleatoric* and *epistemic* uncertainty. In the remainder of this section, we first review classical probabilistic surrogates for operator learning, and then discuss conditional diffusion models as flexible probabilistic surrogates that can represent rich predictive distributions.

### 3.2. Classical Probabilistic Surrogates

A deterministic surrogate, which relies on a point estimate of  $\theta$ , cannot convey predictive uncertainty or indicate when its output may be unreliable. To address this limitation, classical uncertainty quantification adopts Bayesian or ap-

proximate Bayesian perspectives, where a probabilistic surrogate is constructed by learning a posterior distribution over parameters,  $p(\theta \mid \mathcal{D})$ . Under a well-specified prior and likelihood, posterior inference yields uncertainty-aware predictions through the posterior predictive distribution

$$p(u \mid a, \mathcal{D}) = \int p(u \mid a, \theta) p(\theta \mid \mathcal{D}) d\theta.$$

In practice, exact Bayesian inference is often intractable for modern neural networks, so scalable approximations are commonly used, including Monte Carlo dropout (Gal & Ghahramani, 2016) and deep ensembles (Lakshminarayanan et al., 2017).

While these approaches primarily capture *epistemic* uncertainty through parameter uncertainty, they often do not explicitly model *aleatoric* uncertainty, the intrinsic randomness in the conditional output distribution. Moreover, their uncertainty estimates are not necessarily well-calibrated and may require post-hoc calibration techniques (Guo et al., 2017; Kuleshov et al., 2018). As a result, they can be limited when the target variability is irreducible and strongly non-Gaussian, which is common in stochastic PDE settings.

### 3.3. Conditional Diffusion Models as Probabilistic Surrogates

In this work, we interpret conditional diffusion models as implicitly learning an input-conditioned posterior over outputs, denoted by  $p(\theta \mid \mathcal{D}, a)$ . Unlike the Bayesian setting, which seeks a single posterior  $p(\theta \mid \mathcal{D})$  independent of the input, conditional generative models learn a *family* of distributions over  $\theta$  indexed by  $a$ . This makes conditional diffusion models naturally suited to Problem 2.1, where the target is a full conditional distribution and classical Bayesian parameter posteriors do not directly learn aleatoric variability.

Finally, we note that *underfitting* in diffusion training can be linked to *epistemic uncertainty*. In operator learning, data often sparsely cover the conditioning space, so  $\rho_0(\cdot \mid c)$  is reliable near the training support but less certain under extrapolation. When  $\mathcal{L}_V(c)$  remains nonzero, the residual mismatch reflects limited information in  $\mathcal{D}$  and can be interpreted as epistemic uncertainty.

Moreover, if the learned velocity field  $v_\phi$  depends Lipschitz-continuously on the condition  $c$ , then the induced conditional distributions vary in a controlled way: small perturbations of  $c$  lead to small changes in  $\rho_0(\cdot \mid c)$  in  $\mathcal{W}_2$ , while the guarantee naturally weakens as  $c$  moves farther from the training support, aligning with increased epistemic uncertainty under extrapolation. A precise statement and discussion of this conditional stability bound are provided in Appendix A.1.

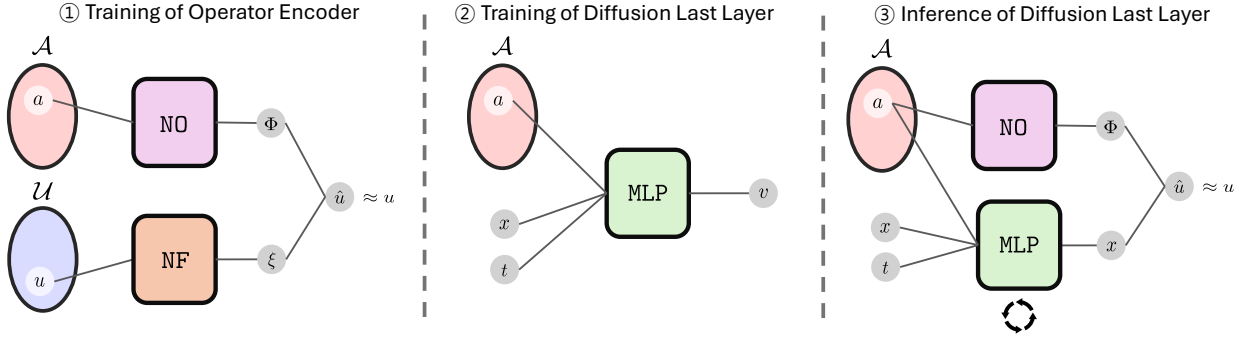


**Figure 2. Training and inference pipeline for the Diffusion Last Layer (DLL).** (1) **Operator encoder.** A NO backbone produces basis functions  $\Phi(a)$  and a NF maps targets to coefficients  $\xi = \text{NF}(u)$ , yielding the low-rank reconstruction  $\hat{u} = \xi^\top \Phi(a)$ . (2) **DLL training.** With the encoder frozen, we train a conditional diffusion model in coefficient space: an MLP denoiser predicts noise (or score) from  $(a, x_t, t)$  using NO features of  $a$  for conditioning. (3) **DLL inference.** For a new input  $a$ , we sample coefficients  $x \sim p(x | a)$  by iterative denoising and decode  $\hat{u} = x^\top \Phi(a)$ .

## 4. Diffusion Last Layer Neural Operators

In this section, we introduce the proposed DLL and summarize its training and inference pipeline in Fig. 2. Following the figure, we first describe the operator encoder and then present the conditional diffusion model that operates in coefficient space.

### 4.1. Operator Encoder

Given the dataset  $\mathcal{D}$  in (1), we learn a conditional encoder–decoder for the target field  $u$  given the input  $a$  using a neural operator feature extractor, which we refer to as an *operator encoder*. Concretely, we represent  $u$  via a rank- $r$  expansion

$$u \approx \hat{u} := \sum_{k=1}^r \xi_k \phi_k = \xi^\top \Phi,$$

where  $\Phi = (\phi_1, \dots, \phi_r) \in \mathcal{U}^r$  denotes a collection of basis functions in  $\mathcal{U}$  produced by the neural operator backbone, and  $\xi = (\xi_1, \dots, \xi_r) \in \mathbb{R}^r$  is an instance-specific coefficient vector.

In our implementation, the coefficients are produced by a neural functional encoder  $\xi = \text{NF}(u)$ , while the basis functions are generated by a neural operator  $\Phi = \text{NO}(a)$  conditioned on the input, yielding the reconstruction  $\hat{u} = \text{NF}(u)^\top \text{NO}(a)$ . This provides a compact conditional representation of the target through  $\xi$ , which we use as the latent variable for diffusion modeling in the next subsection.

We train the operator encoder by minimizing the reconstruction loss

$$\mathcal{L}_{\text{OE}} = \mathbb{E}_{(a, u) \sim \mathcal{D}} \|u - \text{NF}(u)^\top \text{NO}(a)\|_2^2, \quad (5)$$

which encourages  $\xi$  and  $\Phi$  to yield an accurate rank- $r$  approximation of  $u$ . Intuitively, NO( $a$ ) produces an input-dependent basis, while NF( $u$ ) extracts instance-specific co-

efficients, so that their combination reconstructs  $u$  with small mean-squared error.

Under standard approximation assumptions, minimizing (5) recovers the optimal rank- $r$  reconstruction for each fixed input in the  $L^2$  sense.

**Proposition 4.1** (Optimal rank- $r$  reconstruction). *Fix  $r \in \mathbb{N}$  and  $a \in \mathcal{A}$ . Under the assumptions in Appendix A.2, any global minimizer of  $\mathcal{L}_{\text{OE}}$  in (5) achieves*

$$\inf \mathcal{L}_{\text{OE}}(a) = \inf_{\dim(S)=r} \mathbb{E} [\|u - P_S u\|^2 | a],$$

and the minimizing subspace is the rank- $r$  truncated Karhunen–Loëve subspace of the conditional covariance of  $u$  given  $a$ .

A precise statement and proof are deferred to Appendix A.2. As a result, the operator encoder compresses the high-dimensional output field into a compact coefficient vector  $\xi \in \mathbb{R}^r$ , as opposed to conventional, discrete encoders used in latent diffusion. We next model the conditional distribution of  $\xi$  with a diffusion last layer, enabling efficient probabilistic prediction in this latent coefficient space.

Compared to a standard autoencoder, the operator encoder can achieve higher reconstruction accuracy at the same latent dimension because it uses an *input-dependent* basis,  $\Phi = \text{NO}(a)$ . By adapting the reconstruction subspace to the condition  $a$ , more structure is captured by  $\Phi(a)$ , which reduces the burden on the low-dimensional code  $\xi$  and mitigates bottleneck-induced reconstruction error.

### 4.2. Diffusion Last Layer

Given the learned operator encoder, we form the latent dataset in (2) by setting  $c^{(i)} = a^{(i)}$  and  $x^{(i)} = \text{NF}(u^{(i)})$ . Analogous to latent-variable autoencoders, this reduces conditional generation to modeling a distribution in the finite-

dimensional latent space  $\mathbb{R}^r$ , rather than directly in the function space  $\mathcal{U}$ .

We train the diffusion last layer by minimizing the velocity loss  $\mathcal{L}_V$  in (4). In contrast to pixel-space diffusion models, our method operates entirely in the low-dimensional coefficient space during both training and inference, substantially reducing computational cost and improving sampling efficiency. We parameterize the velocity field with an MLP, a standard choice for generative modeling in finite-dimensional vector spaces (Kotelnikov et al., 2023; Li et al., 2024).

Together, Propositions 2.3 and 4.1 justify this construction: Proposition 2.3 implies that minimizing  $\mathcal{L}_V$  yields a diffusion model that matches the conditional latent law of  $x$  in (2) (in Wasserstein distance), while Proposition 4.1 shows that the encoder represents  $u$  through an input-adaptive rank- $r$  truncated Karhunen-Loéve (KL) expansion. Consequently, DLL parameterizes the conditional output distribution via diffusion in the truncated KL coefficient space.

## 5. Experiments

We evaluate DLL on both stochastic and deterministic benchmarks. In all experiments, we use the FNO (Li et al., 2020) as the backbone neural operator NO. The neural functional encoder NF shares the same FNO architecture and applies global average pooling to produce the latent coefficients. Unless stated otherwise, we fix the latent dimension to  $r = 64$  across all benchmarks. Additional implementation details are provided in Appendix B.

### 5.1. Choice of Baselines

We compare DLL against five baselines spanning deterministic prediction, approximate Bayesian uncertainty, and conditional generative modeling. As operator-based references, we include FNO (Li et al., 2020), FNO-d (Monte Carlo dropout at inference), and PNO (Bülte et al., 2025) with a reparameterized latent-variable formulation. We further evaluate two grid-based generative baselines: pixel-space diffusion (DM) and latent diffusion (LDM). Since all benchmarks are defined on regular grids, we focus on these discretized diffusion models (rather than function-space generative approaches) to enable a direct and fair comparison. Additional architectural details are provided in Appendix B.1.

### 5.2. Stochastic Operator Learning

We evaluate whether probabilistic surrogates can capture the aleatoric uncertainty inherent in stochastic PDE data, where each input induces a distribution over outputs. We generate 10,000 training pairs from each stochastic system, and evaluate on 32 test conditions with 64 output realizations per condition. Unless stated otherwise, the 1D Burgers fields

**Table 2. Stochastic Burgers' equation.** Results on distributional and moment metrics. Lower is better. Best and second-best results are highlighted in **bold** and underline, respectively.

Method	ED $\downarrow$	SWD $\downarrow$	NRMSE <sub>m</sub> $\downarrow$	NRMSE <sub>s</sub> $\downarrow$
FNO	6.491	0.426	<b>0.146</b>	1.000
FNO-d	6.075	0.387	0.527	0.755
PNO	1.766	0.253	<u>0.215</u>	0.457
DM	<u>1.355</u>	<u>0.239</u>	0.258	0.323
LDM	1.373	0.249	0.280	<u>0.297</u>
DLL	<b>1.285</b>	<b>0.213</b>	0.252	<b>0.289</b>

are discretized on a uniform grid with  $N_x = 256$  points (i.e.,  $u \in \mathbb{R}^{256}$ ), and the 2D Darcy fields are discretized on a  $128 \times 128$  uniform grid. Full dataset generation details are provided in Appendix B.3.

**Stochastic Burgers' Equation.** We consider the one-dimensional viscous stochastic Burgers' equation on the periodic domain  $x \in [0, 2\pi]$ . The stochastic operator maps an initial condition to the terminal-time solution,  $\mathcal{G}^\dagger : u(\cdot, 0) \mapsto u(\cdot, T)$  for a fixed horizon  $T > 0$ . The dynamics are

$$du = \left(-\frac{1}{2} \partial_x(u^2) + \nu \partial_{xx} u\right) dt + \sum_{j=1}^3 \sigma_j \cos(jx) dW_t^j,$$

where  $\nu > 0$  is the viscosity and  $\{W_t^j\}_{j=1}^3$  are independent standard Brownian motions.

**Stochastic Darcy Flow.** We consider Darcy flow on  $\Omega = (0, 1)^2$ ,

$$-\nabla \cdot (a(x) \nabla u(x)) = f(x), \quad x \in \Omega,$$

where  $a(x)$  is the (input) permeability field and  $u(x)$  is the pressure. Randomness enters through a stochastic source term modeled as a mixture of two Gaussian random fields,

$$f(x) = \lambda \sigma_{\text{ln}} \exp(G_{\text{ln}}(x)) + (1 - \lambda) \sigma_{\text{gp}} G_{\text{gp}}(x),$$

with mixture weight  $\lambda \in [0, 1]$ , scales  $\sigma_{\text{ln}}, \sigma_{\text{gp}} > 0$ , and mean-zero GRFs  $G_{\text{ln}}, G_{\text{gp}}$  (typically independent) with prescribed covariances. This defines a stochastic operator  $\mathcal{G}^\dagger$  mapping  $a$  to a conditional distribution over  $u$ .

**Results.** Across both stochastic benchmarks (Tables 2 and 3), deterministic FNO and FNO-d mainly fit conditional means, yielding low NRMSE<sub>m</sub> but poor recovery of aleatoric variability, as indicated by large ED and SWD and high NRMSE<sub>s</sub>. In contrast, generative surrogates markedly reduce distributional discrepancies, reflecting better alignment with the full conditional law. PNO improves over deterministic baselines but remains weaker on distributional

**Table 3. Stochastic Darcy flow.** Results on distributional and moment metrics. Lower is better. Best and second-best results are highlighted in **bold** and underline, respectively.

Method	ED ↓	SWD ↓	NRMSE <sub>m</sub> ↓	NRMSE <sub>s</sub> ↓
FNO	1.463	0.015	<b>0.253</b>	1.000
FNO-d	1.320	0.014	<u>0.289</u>	0.962
PNO	0.305	0.007	0.388	<u>0.285</u>
DM	<u>0.269</u>	0.007	0.353	0.360
LDM	0.368	<b>0.007</b>	0.610	<b>0.268</b>
DLL	<b>0.227</b>	<u>0.007</u>	0.355	0.357

metrics, suggesting limited capture of fine-grained structure. Overall, **DLL** offers a strong and consistent trade-off across both problems, achieving competitive distributional alignment while matching or exceeding the generalization of pixel-space and latent diffusion baselines in the same regular-grid setting. Definitions of all metrics are provided in Appendix B.4, and qualitative results are shown in Appendix C.1 (Figs. 3 and 4).

### 5.3. Autoregressive Rollout Stability

We next evaluate long-horizon *autoregressive* stability on deterministic chaotic dynamics. Following APEBench (Koehler et al., 2024), we train surrogates for one-step prediction on regular grids and perform *closed-loop* rollouts by recursively feeding predictions back as inputs. This setting directly probes error accumulation and compounding drift over time, a common failure mode of neural emulators in chaotic regimes. In both benchmarks, models are trained on trajectory segments of length 50 and evaluated via closed-loop rollouts of length 100. Full dataset generation details are provided in Appendix B.3.

**Kuramoto–Sivashinsky Equation.** We consider the one-dimensional Kuramoto–Sivashinsky (KS) equation on the periodic domain  $x \in [0, L]$ ,

$$\partial_t u + u \partial_x u + \partial_{xx} u + \partial_{xxxx} u = 0,$$

where the state  $u(\cdot, t)$  is discretized on a uniform grid with  $N_x = 256$  points (i.e.,  $u \in \mathbb{R}^{256}$ ). The autoregressive task is to learn the discrete-time flow map  $u(\cdot, t) \mapsto u(\cdot, t + \Delta t)$  with  $\Delta t = 1$  and assess stability by rolling out predictions over long horizons.

**Kolmogorov Flow.** We also evaluate rollout stability on two-dimensional Kolmogorov flow, modeled by the incompressible Navier–Stokes equations in vorticity form on the periodic domain  $\Omega = (0, 2\pi)^2$ :

$$\partial_t \omega + \mathbf{u} \cdot \nabla \omega = \nu \Delta \omega - \alpha \omega + F(x),$$

$$\Delta \psi = \omega,$$

$$\mathbf{u} = \nabla^\perp \psi,$$

**Table 4. Kuramoto–Sivashinsky equation.** Autoregressive rollout performance. Lower is better for NRMSE and CRPS, and SSR is optimal when close to 1. Best and second-best results are highlighted in **bold** and underline, respectively.

Method	NRMSE ↓	CRPS ↓	SSR → 1
FNO	0.404	—	—
FNO-d	0.384	0.523	<b>0.975</b>
PNO	<u>0.354</u>	<u>0.514</u>	0.550
DM	0.395	<u>0.545</u>	<u>0.961</u>
LDM	0.576	0.878	0.802
DLL	<b>0.343</b>	<b>0.470</b>	0.949

**Table 5. Kolmogorov flow.** Autoregressive rollout performance. Lower is better for NRMSE and CRPS, and SSR is optimal when close to 1. Best and second-best results are highlighted in **bold** and underline, respectively.

Method	NRMSE ↓	CRPS ↓	SSR → 1
FNO	0.528	—	—
FNO-d	0.463	0.912	0.546
PNO	0.492	1.119	0.167
DM	<b>0.369</b>	<b>0.692</b>	<u>0.601</u>
LDM	0.615	1.232	0.548
DLL	<u>0.426</u>	<u>0.822</u>	<b>0.620</b>

where  $\omega$  is the vorticity,  $\psi$  the stream function,  $\nu > 0$  the viscosity, and  $\alpha \geq 0$  the linear drag. We use a single-mode Kolmogorov forcing  $F$ , and discretize  $\omega(\cdot, t)$  on a  $128 \times 128$  uniform grid. Models are trained for one-step prediction with step size  $\Delta t = 0.25$  and evaluated by closed-loop rollouts, which directly tests long-horizon stability under turbulent dynamics.

**Results.** Tables 4 and 5 summarize long-horizon closed-loop rollout performance on KS and Kolmogorov flow. Overall, diffusion-based generative baselines and **DLL** outperform deterministic FNO, indicating improved robustness to compounding errors. On KS, **DLL** achieves the best NRMSE and CRPS while keeping SSR near one, whereas PNO attains competitive NRMSE but shows degraded SSR, suggesting weaker calibration under rollout. On Kolmogorov flow, pixel-space diffusion (DM) yields the strongest accuracy, while **DLL** remains competitive and attains the best SSR, highlighting a favorable accuracy calibration trade-off. In contrast, LDM performs poorly on both systems, suggesting its latent representation does not preserve the fine-scale structure needed for stable long-horizon forecasting. Definitions of all metrics are provided in Appendix B.4, and qualitative results are shown in Appendix C.2 (Figs. 5 and 6).

### 5.4. Reconstruction Property

Tables 6 and 7 show that operator encoder (OE) reconstructs deterministic benchmarks (KS and Kolmogorov flow) more

**Table 6. Reconstruction property (1D).** Autoencoder versus operator encoder. Lower NRMSE indicates better reconstruction.

Encoder	Comp. $\uparrow$	Burgers NRMSE $\downarrow$	KS NRMSE $\downarrow$
AE	$\times 2$	$1.98 \times 10^{-3}$	$7.75 \times 10^{-4}$
OE	$\times 4$	$4.13 \times 10^{-2}$	$2.45 \times 10^{-4}$

**Table 7. Reconstruction property (2D).** Autoencoder versus operator encoder. Lower NRMSE indicates better reconstruction.

Encoder	Comp. $\uparrow$	Darcy NRMSE $\downarrow$	Kolmogorov NRMSE $\downarrow$
AE	$\times 16$	$1.05 \times 10^{-2}$	$3.35 \times 10^{-3}$
OE	$\times 256$	$4.11 \times 10^{-2}$	$3.30 \times 10^{-3}$

accurately than autoencoder (AE), while AE performs better on stochastic benchmarks (Burgers and Darcy). Notably, OE achieves lower error in the deterministic setting despite substantially higher compression ratios, suggesting that operator-conditioned features capture the dominant low-dimensional structure of the solution manifold.

## 6. Related Work and Discussion

**UQ in Operator Learning.** UQ in operator learning has been dominated by approaches targeting *epistemic* uncertainty, including Bayesian neural operators and related approximate Bayesian formulations (Lin et al., 2023; Weber et al., 2024; Magnani et al., 2025a;b), as well as input-perturbation strategies (Pathak et al., 2022). A complementary line models predictive uncertainty through parametric conditional output distributions (Bülte et al., 2025). In contrast, we propose a diffusion-based neural operator framework that learns a flexible conditional generative model and can capture both *aleatoric* variability and *epistemic* uncertainty from data. Separately, recent work has studied calibrated uncertainty sets for neural operators with coverage guarantees via conformal prediction (Ma et al., 2024). Extending such calibration and coverage guarantees to DLL-based surrogates is an important direction for future work.

**Generative Models for Physics.** The use of generative models in the physical sciences has grown rapidly in recent years (Shu et al., 2023; Shysheya et al., 2024; Kohl et al., 24; Zhou et al., 2025a;b; Rozet et al., 2025). Most existing approaches adapt latent-space or pixel-space generative models, often based on U-Nets or diffusion transformers originally developed for vision, to discretized simulation data. In contrast, our work is tailored to operator learning: DLL attaches a conditional generative head directly to a neural-operator backbone, preserving discretization-robust function-to-function prediction while enabling efficient sampling. Moreover, when paired with neural-field or transformer-based operator backbones, DLL naturally extends to Bayesian inverse problems by providing a flexible

conditional prior and likelihood model (Rozet & Louppe, 2023; Huang et al., 2024). Finally, DLL is compatible with emerging large-scale pretrained models for scientific data (Hao et al., 2024; Herde et al., 2024), suggesting a promising route to combine foundation-model representations with principled uncertainty-aware operator emulation.

**Generative Models in Function Spaces.** Recent work formulates diffusion and flow-matching directly over *function-valued* random variables to obtain discretization-robust generative models (Lim et al., 2023; Kerrigan et al., 2023; 2024; Lim et al., 2025; Shi et al., 2025). While DLL performs diffusion in a finite-dimensional coefficient space, it still induces a conditional distribution on  $u \in \mathcal{U}$  via the input-dependent basis, and thus can be viewed as a conditional function generative model implemented through an efficient latent coefficient parameterization.

**Weight Space Uncertainty.** A complementary route to uncertainty quantification models randomness in parameter space. Bayesian neural networks infer a posterior over weights, often via variational methods, to capture epistemic uncertainty (Blundell et al., 2015). For scalability, Bayesian last-layer models restrict posterior inference to the final layer while learning a deterministic feature extractor (Krishtadi et al., 2020; Watson et al., 2021; Harrison et al., 2024). More recently, diffusion models have been used to learn expressive distributions over network weights and enable sampling in weight space (Erkoç et al., 2023; Xie et al., 2024). In contrast, DLL keeps the backbone deterministic and models uncertainty in a low-dimensional output representation, targeting aleatoric variability while remaining complementary to weight-space approaches.

## 7. Conclusion

We introduced the DLL, a simple add-on probabilistic head that turns a deterministic neural operator backbone into a conditional generative surrogate for random field prediction. DLL learns an operator encoder that maps outputs to a compact coefficient representation using an input-dependent basis, then trains a conditional diffusion model in this coefficient space to enable efficient sampling and uncertainty quantification. Across stochastic operator learning benchmarks, DLL improves distributional fidelity and uncertainty calibration relative to deterministic and probabilistic operator baselines, while remaining competitive with grid-based diffusion models. On deterministic chaotic systems, DLL also improves long-horizon autoregressive rollout stability and provides well-calibrated uncertainty under compounding errors. These results suggest DLL as a practical and scalable route to uncertainty-aware operator learning, and motivate future work on principled calibration and extensions to inverse problems and irregular geometries.

## Impact Statement

This paper presents work whose goal is to advance the field of machine learning. There are many potential societal consequences of our work, none of which we feel must be specifically highlighted here.

## Acknowledgment

The work of Sungwon Park was supported by Institute of Information & communications Technology Planning & Evaluation (IITP) grant funded by the Korea government(MSIT) (RS-2022-00143911, AI Excellence Global Innovative Leader Education Program)

## References

Ambrosio, L., Gigli, N., and Savaré, G. *Gradient flows: in metric spaces and in the space of probability measures*. Springer, 2005.

Azizzadenesheli, K., Kovachki, N., Li, Z., Liu-Schiaffini, M., Kossaifi, J., and Anandkumar, A. Neural operators for accelerating scientific simulations and design. *Nature Reviews Physics*, 6(5):320–328, 2024.

Blundell, C., Cornebise, J., Kavukcuoglu, K., and Wierstra, D. Weight uncertainty in neural network. In *International conference on machine learning*, pp. 1613–1622. PMLR, 2015.

Bonev, B., Kurth, T., Hundt, C., Pathak, J., Baust, M., Kashinath, K., and Anandkumar, A. Spherical fourier neural operators: Learning stable dynamics on the sphere. In *International conference on machine learning*, pp. 2806–2823. PMLR, 2023.

Bonnaire, T., Urfin, R., Biroli, G., and Mezard, M. Why diffusion models don’t memorize: The role of implicit dynamical regularization in training. In *The Thirty-ninth Annual Conference on Neural Information Processing Systems*, 2025.

Bülte, C., Scholl, P., and Kutyniok, G. Probabilistic neural operators for functional uncertainty quantification. *Transactions on Machine Learning Research*, 2025. ISSN 2835-8856.

Chen, Y., Goldstein, M., Hua, M., Albergo, M. S., Boffi, N. M., and Vanden-Eijnden, E. Probabilistic forecasting with stochastic interpolants and föllmer processes. In *Proceedings of the 41st International Conference on Machine Learning*, volume 235. PMLR, 2024.

Erkoç, Z., Ma, F., Shan, Q., Nießner, M., and Dai, A. Hyperdiffusion: Generating implicit neural fields with weight-space diffusion. In *Proceedings of the IEEE/CVF international conference on computer vision*, pp. 14300–14310, 2023.

Gal, Y. and Ghahramani, Z. Dropout as a bayesian approximation: Representing model uncertainty in deep learning. In *international conference on machine learning*, pp. 1050–1059. PMLR, 2016.

Gao, R., Hoogeboom, E., Heek, J., De Bortoli, V., Murphy, K. P., and Salimans, T. Diffusion models and gaussian flow matching: Two sides of the same coin. In *The Fourth Blogpost Track at ICLR 2025*, 2025.

Guo, C., Pleiss, G., Sun, Y., and Weinberger, K. Q. On calibration of modern neural networks. In *International conference on machine learning*, pp. 1321–1330. PMLR, 2017.

Hao, Z., Wang, Z., Su, H., Ying, C., Dong, Y., Liu, S., Cheng, Z., Song, J., and Zhu, J. Gnot: A general neural operator transformer for operator learning. In *International Conference on Machine Learning*, pp. 12556–12569. PMLR, 2023.

Hao, Z., Su, C., Liu, S., Berner, J., Ying, C., Su, H., Anandkumar, A., Song, J., and Zhu, J. Dpot: Auto-regressive denoising operator transformer for large-scale pde pre-training. *arXiv preprint arXiv:2403.03542*, 2024.

Harrison, J., Willes, J., and Snoek, J. Variational bayesian last layers. In *The Twelfth International Conference on Learning Representations*, 2024.

Herde, M., Raonic, B., Rohner, T., Käppeli, R., Molinaro, R., de Bézenac, E., and Mishra, S. Poseidon: Efficient foundation models for pdes. *Advances in Neural Information Processing Systems*, 37:72525–72624, 2024.

Ho, J., Jain, A., and Abbeel, P. Denoising diffusion probabilistic models. *Advances in neural information processing systems*, 33:6840–6851, 2020.

Huang, J., Yang, G., Wang, Z., and Park, J. J. Diffusion-pde: Generative pde-solving under partial observation. *Advances in Neural Information Processing Systems*, 37: 130291–130323, 2024.

Kadkhodaie, Z., Guth, F., Simoncelli, E. P., and Mallat, S. Generalization in diffusion models arises from geometry-adaptive harmonic representations. In *The Twelfth International Conference on Learning Representations*, 2024. URL <https://openreview.net/forum?id=ANvmVS2Yr0>.

Kerrigan, G., Ley, J., and Smyth, P. Diffusion generative models in infinite dimensions. In *International Conference on Artificial Intelligence and Statistics*, pp. 9538–9563. PMLR, 2023.

Kerrigan, G., Migliorini, G., and Smyth, P. Functional flow matching. In *Proceedings of The 27th International Conference on Artificial Intelligence and Statistics*, pp. 3934–3942, 2024.

Koehler, F., Niedermayr, S., Thuerey, N., et al. Apebench: A benchmark for autoregressive neural emulators of pdes. *Advances in Neural Information Processing Systems*, 37: 120252–120310, 2024.

Kohl, G., Chen, L., and Thuerey, N. Benchmarking autoregressive conditional diffusion models for turbulent flow simulation. In *ICML 2024 AI for Science Workshop*, 24.

Kotelnikov, A., Baranchuk, D., Rubachev, I., and Babenko, A. Tabddpm: Modelling tabular data with diffusion models. In *International conference on machine learning*, pp. 17564–17579. PMLR, 2023.

Kovachki, N., Li, Z., Liu, B., Azizzadenesheli, K., Bhattacharya, K., Stuart, A., and Anandkumar, A. Neural operator: Learning maps between function spaces with applications to pdes. *Journal of Machine Learning Research*, 24(89):1–97, 2023.

Kristiadi, A., Hein, M., and Hennig, P. Being bayesian, even just a bit, fixes overconfidence in relu networks. In *International conference on machine learning*, pp. 5436–5446. PMLR, 2020.

Kuleshov, V., Fenner, N., and Ermon, S. Accurate uncertainties for deep learning using calibrated regression. In *International conference on machine learning*, pp. 2796–2804. PMLR, 2018.

Kwon, D., Fan, Y., and Lee, K. Score-based generative modeling secretly minimizes the wasserstein distance. *Advances in Neural Information Processing Systems*, 35: 20205–20217, 2022.

Lai, C.-H., Song, Y., Kim, D., Mitsufuji, Y., and Ermon, S. The principles of diffusion models. *arXiv preprint arXiv:2510.21890*, 2025.

Lakshminarayanan, B., Pritzel, A., and Blundell, C. Simple and scalable predictive uncertainty estimation using deep ensembles. *Advances in neural information processing systems*, 30, 2017.

Li, T., Tian, Y., Li, H., Deng, M., and He, K. Autoregressive image generation without vector quantization. *Advances in Neural Information Processing Systems*, 37:56424–56445, 2024.

Li, Z., Kovachki, N., Azizzadenesheli, K., Liu, B., Bhattacharya, K., Stuart, A., and Anandkumar, A. Fourier neural operator for parametric partial differential equations. *arXiv preprint arXiv:2010.08895*, 2020.

Li, Z., Huang, D. Z., Liu, B., and Anandkumar, A. Fourier neural operator with learned deformations for pdes on general geometries. *Journal of Machine Learning Research*, 24(388):1–26, 2023a.

Li, Z., Kovachki, N., Choy, C., Li, B., Kossaifi, J., Otta, S., Nabian, M. A., Stadler, M., Hundt, C., Azizzadenesheli, K., et al. Geometry-informed neural operator for large-scale 3d pdes. *Advances in Neural Information Processing Systems*, 36:35836–35854, 2023b.

Li, Z., Meidani, K., and Farimani, A. B. Transformer for partial differential equations’ operator learning. *Transactions on Machine Learning Research*, 2023c.

Lim, J. H., Kovachki, N. B., Baptista, R., Beckham, C., Azizzadenesheli, K., Kossaifi, J., Voleti, V., Song, J., Kreis, K., Kautz, J., et al. Score-based diffusion models in function space. *Journal of Machine Learning Research*, 26(158):1–62, 2025.

Lim, S., Yoon, E. B., Byun, T., Kang, T., Kim, S., Lee, K., and Choi, S. Score-based generative modeling through stochastic evolution equations in hilbert spaces. *Advances in neural information processing systems*, 36: 37799–37812, 2023.

Lin, G., Moya, C., and Zhang, Z. B-deepnet: An enhanced bayesian deepnet for solving noisy parametric pdes using accelerated replica exchange sgld. *Journal of Computational Physics*, 473:111713, 2023.

Lipman, Y., Chen, R. T. Q., Ben-Hamu, H., Nickel, M., and Le, M. Flow matching for generative modeling. In *The Eleventh International Conference on Learning Representations*, 2023.

Lippe, P., Veeling, B., Perdikaris, P., Turner, R., and Brandstetter, J. Pde-refiner: Achieving accurate long rollouts with neural pde solvers. *Advances in Neural Information Processing Systems*, 36:67398–67433, 2023.

Liu, X., Gong, C., and qiang liu. Flow straight and fast: Learning to generate and transfer data with rectified flow. In *The Eleventh International Conference on Learning Representations*, 2023.

Lu, L., Jin, P., Pang, G., Zhang, Z., and Karniadakis, G. E. Learning nonlinear operators via deepnet based on the universal approximation theorem of operators. *Nature machine intelligence*, 3(3):218–229, 2021.

Ma, Z., Pitt, D., Azizzadenesheli, K., and Anandkumar, A. Calibrated uncertainty quantification for operator learning via conformal prediction. *Transactions on Machine Learning Research*, 2024. ISSN 2835-8856. URL <https://openreview.net/forum?id=cGpegxy12T>.

Magnani, E., Krämer, N., Eschenhagen, R., Rosasco, L., and Hennig, P. Approximate bayesian neural operators: Uncertainty quantification for parametric PDEs. *Transactions on Machine Learning Research*, 2025a. ISSN 2835-8856.

Magnani, E., Pförtner, M., Weber, T., and Hennig, P. Linearization turns neural operators into function-valued gaussian processes. In *Forty-second International Conference on Machine Learning*, 2025b.

Pathak, J., Subramanian, S., Harrington, P., Raja, S., Chattopadhyay, A., Mardani, M., Kurth, T., Hall, D., Li, Z., Azizzadenesheli, K., et al. Fourcastnet: A global data-driven high-resolution weather model using adaptive fourier neural operators. *arXiv preprint arXiv:2202.11214*, 2022.

Price, I., Sanchez-Gonzalez, A., Alet, F., Andersson, T. R., El-Kadi, A., Masters, D., Ewalds, T., Stott, J., Mohamed, S., Battaglia, P., et al. Probabilistic weather forecasting with machine learning. *Nature*, 637(8044):84–90, 2025.

Psaros, A. F., Meng, X., Zou, Z., Guo, L., and Karniadakis, G. E. Uncertainty quantification in scientific machine learning: Methods, metrics, and comparisons. *Journal of Computational Physics*, 477:111902, 2023.

Rahman, M. A., Florez, M. A., Anandkumar, A., Ross, Z. E., and Azizzadenesheli, K. Generative adversarial neural operators. *Transactions on Machine Learning Research*, 2022. ISSN 2835-8856. URL <https://openreview.net/forum?id=X1VzbBU6xZ>.

Rahman, M. A., Ross, Z. E., and Azizzadenesheli, K. U-NO: U-shaped neural operators. *Transactions on Machine Learning Research*, 2023. ISSN 2835-8856.

Rozet, F. and Louppe, G. Score-based data assimilation. *Advances in Neural Information Processing Systems*, 36: 40521–40541, 2023.

Rozet, F., Ohana, R., McCabe, M., Louppe, G., Lanusse, F., and Ho, S. Lost in latent space: An empirical study of latent diffusion models for physics emulation. *arXiv preprint arXiv:2507.02608*, 2025.

Salvi, C., Lemercier, M., and Gerasimovics, A. Neural stochastic pdes: Resolution-invariant learning of continuous spatiotemporal dynamics. *Advances in Neural Information Processing Systems*, 35:1333–1344, 2022.

Shi, Y., Ross, Z. E., Asimaki, D., and Azizzadenesheli, K. Stochastic process learning via operator flow matching. In *The Thirty-ninth Annual Conference on Neural Information Processing Systems*, 2025.

Shu, D., Li, Z., and Farimani, A. B. A physics-informed diffusion model for high-fidelity flow field reconstruction. *Journal of Computational Physics*, 478:111972, 2023.

Shysheya, A., Diaconu, C., Bergamin, F., Perdikaris, P., Hernández-Lobato, J. M., Turner, R., and Mathieu, E. On conditional diffusion models for pde simulations. *Advances in Neural Information Processing Systems*, 37: 23246–23300, 2024.

Sohl-Dickstein, J., Weiss, E., Maheswaranathan, N., and Ganguli, S. Deep unsupervised learning using nonequilibrium thermodynamics. In *International conference on machine learning*, pp. 2256–2265. pmlr, 2015.

Song, K., Kim, J., Chen, S., Du, Y., Kakade, S., and Sitzmann, V. Selective underfitting in diffusion models. *arXiv preprint arXiv:2510.01378*, 2025.

Song, Y., Sohl-Dickstein, J., Kingma, D. P., Kumar, A., Ermon, S., and Poole, B. Score-based generative modeling through stochastic differential equations. In *International Conference on Learning Representations*, 2021.

Tran, A., Mathews, A., Xie, L., and Ong, C. S. Factorized fourier neural operators. In *The Eleventh International Conference on Learning Representations*, 2023.

Wang, S., Wu, Z., van Dijk, D., and Lu, L. Geofunflow: Geometric function flow matching for inverse operator learning over complex geometries. *arXiv preprint arXiv:2509.24117*, 2025.

Watson, J., Lin, J. A., Klink, P., Pajarinen, J., and Peters, J. Latent derivative bayesian last layer networks. In *International Conference on Artificial Intelligence and Statistics*, pp. 1198–1206. PMLR, 2021.

Weber, T., Magnani, E., Pförtner, M., and Hennig, P. Uncertainty quantification for fourier neural operators. In *ICLR 2024 workshop on AI4DifferentialEquations in science*, 2024.

Xie, M., Li, S., Xie, B., Liu, C., Liang, J., Sun, Z., Feng, K., and Zhu, C. Weight diffusion for future: Learn to generalize in non-stationary environments. *Advances in Neural Information Processing Systems*, 37:6367–6392, 2024.

Xiu, D. *Numerical methods for stochastic computations: a spectral method approach*. Princeton university press, 2010.

Zhou, A., Li, Z., Schneier, M., Jr, J. R. B., and Farimani, A. B. Text2PDE: Latent diffusion models for accessible physics simulation. In *The Thirteenth International Conference on Learning Representations*, 2025a.

Zhou, A., Wikner, A., Lancelin, A., Hassanzadeh, P., and Farimani, A. B. Reframing generative models for physical systems using stochastic interpolants. *arXiv preprint arXiv:2509.26282*, 2025b.

## A. Theoretical Analysis

### A.1. UQ with Diffusion Models

In this section, we discuss how diffusion model training with velocity targets connects to uncertainty quantification. Because our setting includes both distributional targets and point mass targets, we formulate stability in the Wasserstein metric, for which KL divergence is not well suited. Following Kwon et al. (2022), we establish a Wasserstein stability estimate for the continuity equation.

First, to ensure well-posedness, we impose standard integrability and Lipschitz regularity conditions on the velocity fields.

**Assumption A.1** (Integrability and Lipschitz regularity). For  $i \in \{1, 2\}$ , let  $(\rho_t^{(i)})_{t \in [0, T]}$  be narrowly continuous probability measures on  $\mathbb{R}^d$  with finite second moment. Let  $v_t^{(i)} : \mathbb{R}^d \rightarrow \mathbb{R}^d$  be Borel vector fields such that

$$\int_0^T \int_{\mathbb{R}^d} \|v_t^{(i)}(x)\|^2 d\rho_t^{(i)}(x) dt < \infty, \quad i \in \{1, 2\}, \quad (6)$$

$$\|v_t^{(1)}(x) - v_t^{(1)}(y)\| \leq L(t) \|x - y\| \quad \text{for a.e. } t \in [0, T], \quad \forall x, y \in \mathbb{R}^d, \quad (7)$$

for some  $L \in L^1(0, T)$ . Moreover,  $\rho_t^{(i)}$  solves the continuity equation

$$\partial_t \rho_t^{(i)} + \nabla \cdot (\rho_t^{(i)} v_t^{(i)}) = 0, \quad \rho_T^{(i)}(\cdot | c) = p_{\text{noise}}(\cdot), \quad i \in \{1, 2\}. \quad (8)$$

We establish a backward-in-time differential inequality controlling the evolution of the Wasserstein distance between two continuity equation solutions in terms of the velocity field mismatch and the Lipschitz regularity.

**Lemma A.2** (Differential inequality). *Under Assumption A.1, for a.e.  $t \in [0, T]$ ,*

$$-\frac{d}{dt} \mathcal{W}_2(\rho_t^{(1)}, \rho_t^{(2)}) \leq \left( \mathbb{E}_{x \sim \rho_t^{(2)}} [\|v_t^{(2)}(x) - v_t^{(1)}(x)\|^2] \right)^{1/2} + L(t) \mathcal{W}_2(\rho_t^{(1)}, \rho_t^{(2)}). \quad (9)$$

*Proof.* Let  $\pi_t \in \Pi(\rho_t^{(1)}, \rho_t^{(2)})$  be an optimal coupling for the quadratic cost, so that  $\mathcal{W}_2^2(\rho_t^{(1)}, \rho_t^{(2)}) = \int \|x - y\|^2 d\pi_t(x, y)$ . By Theorem 8.4.7 in Ambrosio et al. (2005),

$$-\frac{d}{dt} \frac{1}{2} \mathcal{W}_2^2(\rho_t^{(1)}, \rho_t^{(2)}) = \mathbb{E}_{(x, y) \sim \pi_t} [(x - y) \cdot (v_t^{(2)}(y) - v_t^{(1)}(x))]. \quad (10)$$

Add and subtract  $v_t^{(1)}(y)$ :

$$(x - y) \cdot (v_t^{(2)}(y) - v_t^{(1)}(x)) = (x - y) \cdot (v_t^{(1)}(y) - v_t^{(1)}(x)) + (x - y) \cdot (v_t^{(2)}(y) - v_t^{(1)}(y)). \quad (11)$$

For the first term, using Cauchy–Schwarz and (7),

$$\begin{aligned} \mathbb{E}_{\pi_t} [(x - y) \cdot (v_t^{(1)}(y) - v_t^{(1)}(x))] &\leq \mathbb{E}_{\pi_t} [\|x - y\| \|v_t^{(1)}(y) - v_t^{(1)}(x)\|] \\ &\leq L(t) \mathbb{E}_{\pi_t} \|x - y\|^2. \end{aligned} \quad (12)$$

For the second term, Cauchy–Schwarz gives

$$\mathbb{E}_{\pi_t} [(x - y) \cdot (v_t^{(2)}(y) - v_t^{(1)}(y))] \leq \left( \mathbb{E}_{\pi_t} \|x - y\|^2 \right)^{1/2} \left( \mathbb{E}_{\pi_t} \|v_t^{(2)}(y) - v_t^{(1)}(y)\|^2 \right)^{1/2}. \quad (13)$$

Since the  $y$ -marginal of  $\pi_t$  is  $\rho_t^{(2)}$ ,

$$\mathbb{E}_{\pi_t} \|v_t^{(2)}(y) - v_t^{(1)}(y)\|^2 = \mathbb{E}_{y \sim \rho_t^{(2)}} \|v_t^{(2)}(y) - v_t^{(1)}(y)\|^2. \quad (14)$$

Combining (10)–(14) and using  $\mathbb{E}_{\pi_t} \|x - y\|^2 = \mathcal{W}_2^2(\rho_t^{(1)}, \rho_t^{(2)})$  yields

$$-\frac{d}{dt} \frac{1}{2} \mathcal{W}_2^2(\rho_t^{(1)}, \rho_t^{(2)}) \leq L(t) \mathcal{W}_2^2(\rho_t^{(1)}, \rho_t^{(2)}) + \mathcal{W}_2(\rho_t^{(1)}, \rho_t^{(2)}) \|v_t^{(2)} - v_t^{(1)}\|_{L^2(\rho_t^{(2)})}.$$

Dividing by  $\mathcal{W}_2(\rho_t^{(1)}, \rho_t^{(2)})$  (the case  $\mathcal{W}_2 = 0$  is trivial) gives (9).  $\square$

Integrating Lemma A.2 backward from the shared terminal condition  $\rho_T^{(1)} = \rho_T^{(2)}$  yields an explicit stability bound at  $t = 0$ , controlled by the time-accumulated velocity mismatch with a Grönwall weight.

**Proposition A.3** (Integrated stability bound). *Under Assumption A.1, define  $\Lambda(t) := \int_0^t L(s) ds$ . Then*

$$\mathcal{W}_2(\rho_0^{(1)}, \rho_0^{(2)}) \leq \int_0^T \exp(\Lambda(t)) \left( \mathbb{E}_{x \sim \rho_t^{(2)}} [\|v_t^{(2)}(x) - v_t^{(1)}(x)\|^2] \right)^{1/2} dt. \quad (15)$$

In particular, by Cauchy–Schwarz,

$$\mathcal{W}_2(\rho_0^{(1)}, \rho_0^{(2)}) \leq \left( \int_0^T \exp(2\Lambda(t)) dt \right)^{1/2} \left( \int_0^T \mathbb{E}_{x \sim \rho_t^{(2)}} [\|v_t^{(2)}(x) - v_t^{(1)}(x)\|^2] dt \right)^{1/2}. \quad (16)$$

*Proof.* Let  $D(t) := \mathcal{W}_2(\rho_t^{(1)}, \rho_t^{(2)})$  and  $E(t) := \|v_t^{(2)} - v_t^{(1)}\|_{L^2(\rho_t^{(2)})}$ . Lemma A.2 implies  $D'(t) \leq E(t) + L(t)D(t)$  for a.e.  $t$ . Multiplying by  $\exp(-\Lambda(t))$  gives

$$\frac{d}{dt} \left( \exp(-\Lambda(t)) D(t) \right) \leq \exp(-\Lambda(t)) E(t). \quad (17)$$

Integrating (17) from 0 to  $T$  and using  $D(T) = \mathcal{W}_2(\rho_T^{(1)}, \rho_T^{(2)}) = 0$  because both terminal measures equal  $p_{\text{noise}}$  yields

$$D(0) \leq \int_0^T \exp(\Lambda(t)) E(t) dt, \quad (18)$$

which is (15). Applying Cauchy–Schwarz in time gives (16).  $\square$

We apply Proposition A.3 to relate the Wasserstein error at  $t = 0$  to the velocity-matching error along the forward noising marginals, yielding  $\mathcal{W}_2(p(\cdot | c), \rho_0(\cdot | c)) \lesssim \sqrt{\mathcal{L}_V(c)}$  up to a Grönwall factor.

*Proof of Proposition 2.3.* Fix  $c$  and let  $\rho_t^*(\cdot | c)$  denote the forward marginals induced by (3), so that  $\rho_0^*(\cdot | c) = p(\cdot | c)$  and  $\rho_T^*(\cdot | c) = p_{\text{noise}}$ . Let  $v^*(\cdot, t, c)$  be the corresponding oracle velocity field, and let  $\rho_t(\cdot | c)$  be the solution of the continuity equation driven by the learned velocity  $v_\phi(\cdot, t, c)$  with the same terminal condition  $\rho_T(\cdot | c) = p_{\text{noise}}$ . Under the regularity assumptions of Proposition A.3, applying (16) with  $(\rho_t^{(1)}, v_t^{(1)}) = (\rho_t, v_\phi)$  and  $(\rho_t^{(2)}, v_t^{(2)}) = (\rho_t^*, v^*)$  yields

$$\begin{aligned} \mathcal{W}_2(p(\cdot | c), \rho_0(\cdot | c)) &= \mathcal{W}_2(\rho_0^*(\cdot | c), \rho_0(\cdot | c)) \\ &\leq \left( \int_0^T \exp(2\Lambda(t)) dt \right)^{1/2} \left( \int_0^T \mathbb{E}_{x \sim \rho_t^*(\cdot | c)} [\|v_\phi(x, t, c) - v^*(x, t, c)\|^2] dt \right)^{1/2}, \end{aligned}$$

where  $\Lambda(t) = \int_0^t L(s) ds$ . Recalling the velocity-matching objective (4), we have

$$\int_0^T \mathbb{E}_{x \sim \rho_t^*(\cdot | c)} [\|v_\phi(x, t, c) - v^*(x, t, c)\|^2] dt = \mathcal{L}_V(c).$$

Therefore,

$$\mathcal{W}_2(p(\cdot | c), \rho_0(\cdot | c)) \leq C \sqrt{\mathcal{L}_V(c)}, \quad C := \left( \int_0^T \exp(2\Lambda(t)) dt \right)^{1/2},$$

which proves the claim.  $\square$

To connect diffusion learning with epistemic uncertainty, we require that the learned velocity field varies smoothly with the condition: a Lipschitz dependence on  $c$  ensures that nearby conditions induce similar transport dynamics, so uncertainty inferred at training conditions propagates continuously to unseen but nearby conditions.

**Assumption A.4** (Lipschitz continuity in the condition). There exists  $L_c > 0$  such that for all  $c_1, c_2$ , a.e.  $t \in [0, T]$ , and all  $x \in \mathbb{R}^d$ ,

$$\|v_\phi(x, t, c_1) - v_\phi(x, t, c_2)\| \leq L_c \|c_1 - c_2\|.$$

Under the Lipschitz dependence in Assumption A.4, the reverse-time flow inherits a quantitative continuity with respect to the condition: perturbing  $c$  by a small amount changes the generated distribution at  $t = 0$  by at most a proportional amount in  $\mathcal{W}_2$ , with a constant determined by the Lipschitz regularity of the velocity field.

**Proposition A.5** (Conditional stability). *Under Assumptions A.1 and A.4, letting  $\Lambda(t) := \int_0^t L(s) ds$ , we have*

$$\mathcal{W}_2(\rho_0(\cdot | c_1), \rho_0(\cdot | c_2)) \leq \left( L_c \int_0^T \exp(\Lambda(t)) dt \right) \|c_1 - c_2\|.$$

*Proof.* Apply Proposition A.3 with  $(\rho_t^{(1)}, v_t^{(1)}) = (\rho_t(\cdot | c_1), v_\phi(\cdot, t, c_1))$  and  $(\rho_t^{(2)}, v_t^{(2)}) = (\rho_t(\cdot | c_2), v_\phi(\cdot, t, c_2))$ :

$$\mathcal{W}_2(\rho_0(\cdot | c_1), \rho_0(\cdot | c_2)) \leq \int_0^T \exp(\Lambda(t)) \left( \mathbb{E}_{x \sim \rho_t(\cdot | c_2)} [\|v_\phi(x, t, c_2) - v_\phi(x, t, c_1)\|^2] \right)^{1/2} dt.$$

By Assumption A.4,

$$\left( \mathbb{E}_{x \sim \rho_t(\cdot | c_2)} [\|v_\phi(x, t, c_2) - v_\phi(x, t, c_1)\|^2] \right)^{1/2} \leq L_c \|c_2 - c_1\|.$$

Substituting this bound yields the claim.  $\square$

Proposition A.5 formalizes *conditional stability*: small perturbations of the condition produce proportionally small changes in the generated law at  $t = 0$  in  $\mathcal{W}_2$ . In particular, for an unseen condition  $c_2$  close to a training condition  $c_1$ , the model distribution  $\rho_0(\cdot | c_2)$  remains close to  $\rho_0(\cdot | c_1)$ , whereas for conditions far from the training support the Lipschitz bound becomes less informative, aligning with the expected growth of epistemic uncertainty under extrapolation.

## A.2. Diffusion Last Layer

We first formalize the operator encoder reconstruction problem at a fixed condition  $a$  in an abstract Hilbert space setting. This isolates the geometric content of rank- $r$  approximation independently of any particular parameterization.

**Assumption A.6** (Hilbert setting and conditional second moments). Let  $\mathcal{U}$  be a separable Hilbert space with inner product  $\langle \cdot, \cdot \rangle$  and norm  $\| \cdot \|$ . Fix an input  $a \in \mathcal{A}$  and let  $u$  be a  $\mathcal{U}$ -valued random element under the conditional law  $\mathbb{P}(\cdot | a)$  such that  $\mathbb{E}[\|u\|^2 | a] < \infty$ . Let  $\Phi(a) = (\phi_1(a), \dots, \phi_r(a)) \in \mathcal{U}^r$  define the  $r$ -dimensional subspace  $S(a) := \text{span}\{\phi_1(a), \dots, \phi_r(a)\} \subset \mathcal{U}$ , and let  $P_{S(a)} : \mathcal{U} \rightarrow S(a)$  denote the orthogonal projector.

Our first step is a Pythagorean decomposition of the reconstruction error into an irreducible approximation term, the distance to the chosen subspace, and an estimation term capturing how well the encoder matches the orthogonal projection.

**Lemma A.7** (Projection decomposition). *Under Assumption A.6, for any measurable map  $\hat{u} : \mathcal{U} \rightarrow S(a)$ ,*

$$\|u - \hat{u}(u)\|^2 = \|u - P_{S(a)}u\|^2 + \|P_{S(a)}u - \hat{u}(u)\|^2, \quad \mathbb{P}(\cdot | a)\text{-a.s.}$$

Consequently,

$$\mathbb{E}[\|u - \hat{u}(u)\|^2 | a] = \mathbb{E}[\|u - P_{S(a)}u\|^2 | a] + \mathbb{E}[\|P_{S(a)}u - \hat{u}(u)\|^2 | a].$$

*Proof.* Since  $u - P_{S(a)}u \perp S(a)$  and  $P_{S(a)}u - \hat{u}(u) \in S(a)$ , the cross term vanishes:  $\langle u - P_{S(a)}u, P_{S(a)}u - \hat{u}(u) \rangle = 0$ . Expanding  $\|u - \hat{u}(u)\|^2 = \|(u - P_{S(a)}u) + (P_{S(a)}u - \hat{u}(u))\|^2$  yields the identity; taking conditional expectations gives the second claim.  $\square$

With the subspace  $S(a)$  fixed, we can characterize the optimal encoder: minimizing the conditional mean-squared reconstruction error forces the reconstruction to coincide with the orthogonal projection onto  $S(a)$ .

**Proposition A.8** (Fixed basis: optimal encoder equals orthogonal projection). *Fix  $a$  and  $\Phi(a)$  as in Assumption A.6. Consider the reconstruction model  $\hat{u}_\xi(u) = \sum_{k=1}^r \xi_k(u) \phi_k(a) \in S(a)$  with a measurable encoder  $\xi : \mathcal{U} \rightarrow \mathbb{R}^r$ , and the conditional risk*

$$\mathcal{L}(\xi; a, \Phi) := \mathbb{E}[\|u - \hat{u}_\xi(u)\|^2 \mid a].$$

Then

$$\inf_{\xi} \mathcal{L}(\xi; a, \Phi) = \mathbb{E}[\|u - P_{S(a)}u\|^2 \mid a],$$

and any minimizer satisfies  $\hat{u}_{\xi^*}(u) = P_{S(a)}u$   $\mathbb{P}(\cdot \mid a)$ -a.s. In particular, if the Gram matrix  $G \in \mathbb{R}^{r \times r}$  with  $G_{ij} = \langle \phi_i(a), \phi_j(a) \rangle$  is invertible, then the (a.s.) unique coefficient vector of the minimizer is

$$\xi^*(u) = G^{-1}b(u), \quad b_i(u) = \langle u, \phi_i(a) \rangle.$$

*Proof.* Apply Lemma A.7 with  $\hat{u} = \hat{u}_\xi$ , which implies  $\mathcal{L}(\xi; a, \Phi) \geq \mathbb{E}[\|u - P_{S(a)}u\|^2 \mid a]$  with equality iff  $\hat{u}_\xi(u) = P_{S(a)}u$  a.s. When  $G$  is invertible, the coefficients of  $P_{S(a)}u$  in the spanning set  $\{\phi_k(a)\}$  solve the normal equations  $G\xi = b(u)$ , yielding  $\xi^*(u) = G^{-1}b(u)$ .  $\square$

To identify which subspace is optimal, we introduce the conditional covariance operator associated with the centered random field under  $\mathbb{P}(\cdot \mid a)$ , which provides a spectral description of the conditional variability.

**Lemma A.9** (Conditional covariance operator). *Under Assumption A.6, define the conditional mean  $\mu(a) := \mathbb{E}[u \mid a] \in \mathcal{U}$  and centered random element  $\tilde{u} := u - \mu(a)$ . The conditional covariance operator  $C_a : \mathcal{U} \rightarrow \mathcal{U}$  defined by*

$$C_a f := \mathbb{E}[\langle \tilde{u}, f \rangle \tilde{u} \mid a]$$

is self-adjoint, positive semidefinite, and trace-class, with  $\text{tr}(C_a) = \mathbb{E}[\|\tilde{u}\|^2 \mid a]$ . Therefore  $C_a$  admits an orthonormal eigenbasis  $(e_k(a))_{k \geq 1}$  with eigenvalues  $\lambda_1(a) \geq \lambda_2(a) \geq \dots \geq 0$ .

*Proof.* Linearity of conditional expectation implies that  $C_a$  is linear. For  $f, g \in \mathcal{U}$ ,

$$\langle C_a f, g \rangle = \left\langle \mathbb{E}[\langle \tilde{u}, f \rangle \tilde{u} \mid a], g \right\rangle = \mathbb{E}[\langle \tilde{u}, f \rangle \langle \tilde{u}, g \rangle \mid a] = \langle f, C_a g \rangle,$$

so  $C_a$  is self-adjoint. Moreover,

$$\langle C_a f, f \rangle = \mathbb{E}[\langle \tilde{u}, f \rangle^2 \mid a] \geq 0,$$

hence  $C_a$  is positive semidefinite. Let  $\{e_k\}_{k \geq 1}$  be an orthonormal basis of  $\mathcal{U}$ . Then

$$\sum_{k \geq 1} \langle C_a e_k, e_k \rangle = \mathbb{E} \left[ \sum_{k \geq 1} \langle \tilde{u}, e_k \rangle^2 \mid a \right] = \mathbb{E}[\|\tilde{u}\|^2 \mid a] < \infty,$$

where we used monotone convergence and Parseval's identity. Thus  $C_a$  is trace-class and  $\text{tr}(C_a) = \mathbb{E}[\|\tilde{u}\|^2 \mid a]$ . Being self-adjoint and trace-class,  $C_a$  is compact, so the spectral theorem yields an orthonormal eigenbasis  $(e_k(a))_{k \geq 1}$  with eigenvalues  $\lambda_k(a) \geq 0$ .  $\square$

The covariance spectrum yields the best rank- $r$  subspace in the mean-squared sense: the truncated KL subspace maximizes captured variance and minimizes the residual energy.

**Proposition A.10** (Optimal basis: truncated conditional KL subspace). *Fix  $a$  and consider centered reconstruction of  $\tilde{u} = u - \mu(a)$ . Among all  $r$ -dimensional subspaces  $S \subset \mathcal{U}$ ,*

$$\inf_{\dim(S)=r} \mathbb{E}[\|\tilde{u} - P_S \tilde{u}\|^2 \mid a] = \sum_{k>r} \lambda_k(a),$$

where  $(\lambda_k(a), e_k(a))_{k \geq 1}$  are the eigenpairs of  $C_a$  from Lemma A.9. Moreover, the infimum is attained by the truncated Karhunen–Loëve subspace

$$S^*(a) := \text{span}\{e_1(a), \dots, e_r(a)\}, \quad \text{equivalently} \quad P_{S^*(a)} = \sum_{k=1}^r e_k(a) \otimes e_k(a).$$

*Proof.* For any orthogonal projector  $P_S$ , idempotence and self-adjointness give  $\|\tilde{u} - P_S \tilde{u}\|^2 = \|\tilde{u}\|^2 - \|P_S \tilde{u}\|^2$ . Taking conditional expectations yields

$$\mathbb{E}[\|\tilde{u} - P_S \tilde{u}\|^2 | a] = \mathbb{E}[\|\tilde{u}\|^2 | a] - \mathbb{E}[\|P_S \tilde{u}\|^2 | a].$$

Let  $\{s_i\}_{i=1}^r$  be an orthonormal basis of  $S$ . Then  $\mathbb{E}[\|P_S \tilde{u}\|^2 | a] = \sum_{i=1}^r \mathbb{E}[\langle \tilde{u}, s_i \rangle^2 | a] = \sum_{i=1}^r \langle C_a s_i, s_i \rangle = \text{tr}(P_S C_a)$ . By Ky Fan's maximum principle for compact self-adjoint operators,  $\sup_{\dim(S)=r} \text{tr}(P_S C_a) = \sum_{k=1}^r \lambda_k(a)$ , attained by  $S^*(a) = \text{span}\{e_1(a), \dots, e_r(a)\}$ . Finally,  $\mathbb{E}[\|\tilde{u}\|^2 | a] = \text{tr}(C_a) = \sum_{k \geq 1} \lambda_k(a)$ , hence the minimum equals  $\sum_{k>r} \lambda_k(a)$ .  $\square$

We now connect these functional analytic characterizations to the learnable operator encoder architecture by assuming sufficient expressivity of the neural operator basis map and the coefficient encoder at the fixed input  $a$ .

**Assumption A.11** (Universal approximation for the operator encoder). Let  $\mathcal{A}$  and  $\mathcal{U}$  be separable Hilbert spaces and fix  $r \in \mathbb{N}$ . Fix an input  $a \in \mathcal{A}$  and assume  $\mathbb{E}[\|u\|^2 | a] < \infty$ . Consider parametrized maps  $\text{NO}_\psi : \mathcal{A} \rightarrow \mathcal{U}^r$  and  $\text{NF}_\varphi : \mathcal{U} \rightarrow \mathbb{R}^r$ . Assume:

1. (*Universal basis at fixed  $a$* ) For every  $r$ -dimensional subspace  $S \subset \mathcal{U}$ , there exists  $\psi$  such that

$$\text{span}(\text{NO}_\psi(a)) = S.$$

2. (*Universal coefficients*) For every  $\Psi \in \mathcal{U}^r$  with  $S = \text{span}(\Psi)$ , there exists  $\varphi$  such that

$$\text{NF}_\varphi(u)^\top \Psi = P_S u, \quad \mathbb{P}(\cdot | a)\text{-a.s.},$$

where  $P_S : \mathcal{U} \rightarrow S$  denotes the orthogonal projector onto  $S$ .

Under this universal approximation assumption, the training objective reduces to choosing a subspace and then projecting onto it: optimizing the coefficient network recovers the projection for a fixed basis, and optimizing the basis network recovers an optimal rank- $r$  subspace.

*Proof of Proposition 4.1.* Fix  $\psi$  and define

$$\Psi := \text{NO}_\psi(a) \in \mathcal{U}^r, \quad S := \text{span}(\Psi) \subset \mathcal{U}.$$

For any  $\varphi$ , the reconstruction

$$\hat{u}_{\psi, \varphi}(u, a) := \text{NF}_\varphi(u)^\top \Psi$$

lies in  $S$   $\mathbb{P}(\cdot | a)$ -a.s.; hence Proposition A.8 implies

$$\mathcal{L}_{\text{OE}}(\psi, \varphi; a) := \mathbb{E}[\|u - \hat{u}_{\psi, \varphi}(u, a)\|^2 | a] \geq \mathbb{E}[\|u - P_S u\|^2 | a], \quad \forall \varphi. \quad (19)$$

On the other hand, by Assumption A.11, there exists  $\varphi_S$  such that

$$\hat{u}_{\psi, \varphi_S}(u, a) = P_S u, \quad \mathbb{P}(\cdot | a)\text{-a.s.},$$

which yields

$$\inf_{\varphi} \mathcal{L}_{\text{OE}}(\psi, \varphi; a) \leq \mathcal{L}_{\text{OE}}(\psi, \varphi_S; a) = \mathbb{E}[\|u - P_S u\|^2 | a]. \quad (20)$$

Combining (19) and (20) gives

$$\inf_{\varphi} \mathcal{L}_{\text{OE}}(\psi, \varphi; a) = \mathbb{E}[\|u - P_{\text{span}(\text{NO}_\psi(a))} u\|^2 | a]. \quad (21)$$

Minimizing (21) over  $\psi$  and using Assumption A.11 yields

$$\inf_{\psi, \varphi} \mathcal{L}_{\text{OE}}(\psi, \varphi; a) = \inf_{\dim(S)=r} \mathbb{E}[\|u - P_S u\|^2 | a].$$

Finally, any global minimizer of  $\mathcal{L}_{\text{OE}}(\psi, \varphi; a)$  attains this infimum, proving the claim.  $\square$

Table 8. Backbone parameter counts (millions) for 1D and 2D experiments.

	FNO	FNO-d	PNO	DM	LDM	DLL
1D	0.329M	0.329M	0.329M	3.732M	3.733M	2.117M
2D	8.964M	8.964M	8.964M	34.646M	34.665M	10.751M

Table 9. Encoder parameter counts (millions) for latent representations: AE used by LDM and OE used by DLL.

	LDM (AE)	DLL (OE)
1D	3.421M	0.675M
2D	9.743M	17.944M

## B. Experimental Details

### B.1. Architectural Details

**FNO backbone.** Across all benchmarks, we use the Fourier Neural Operator (FNO) (Li et al., 2020) as the backbone neural operator. We employ 4 Fourier layers with hidden width 64, and retain 32 Fourier modes per spatial dimension (i.e., [32] in 1D and [32, 32] in 2D). Unless stated otherwise, the backbone maps  $1 \rightarrow 1$  channels, and the same architecture is reused as a feature extractor when constructing conditioning embeddings.

**FNO with dropout.** For the Monte Carlo dropout baseline (FNO-d), we use the same FNO architecture and enable dropout in the channel-MLP blocks during inference (dropout probability  $p = 0.2$ ). Predictive distributions are approximated by sampling an ensemble (typically  $K = 32$  forward passes).

**PNO.** For probabilistic operator baselines, we adopt a reparameterized latent-variable formulation (PNO) built on an FNO backbone. The model outputs two channels corresponding to a location and scale parameterization and is trained with an energy-score objective, using a small number of samples per training example (default 8) and a larger ensemble at evaluation (typically  $K = 32$ ).

**DM and LDM.** For grid-based generative baselines, we consider pixel-space diffusion (DM) and latent diffusion (LDM). DM uses conditional U-Net backbones (1D and 2D variants) trained by flow matching with horizon  $T = 10$ . LDM follows a two-stage pipeline: we first train an autoencoder (VAE-style) to obtain a compact latent representation of the target field, and then train a conditional U-Net in latent space under the same flow-matching objective. Conditioning is done by concatenating the condition features with the network input.

**DLL.** For DLL, we first train the operator encoder: an FNO-based operator backbone produces an input-dependent basis, and a neural functional encoder maps target fields to coefficient vectors of dimension  $r = 64$ . We then freeze the operator encoder and train the diffusion last layer in coefficient space using a conditional MLP velocity model (three hidden layers of width 512, time-embedding dimension 32) conditioned on FNO features. We use  $T = 10$  and draw  $K = 32$  samples at evaluation unless stated otherwise.

**Parameter Counts** Tables 8 and 9 report trainable parameter counts, split into backbone models and encoders for latent representations. In Table 8, FNO, FNO-d, and PNO use the same parameter budget within each dimension, enabling controlled comparisons. Diffusion baselines (DM and LDM) are larger, especially in 2D, whereas DLL remains more parameter-efficient. Table 9 lists the additional encoder parameters, where LDM uses an autoencoder (AE) and DLL uses an operator encoder (OE).

### B.2. Training Configurations

**Optimization and normalization.** All models are trained with AdamW (learning rate  $10^{-3}$ ) and cosine learning-rate annealing, with gradient clipping at 1.0. We apply standard Gaussian normalization to inputs and outputs. For generative baselines (DM, LDM, and DLL), we use EMA with decay 0.999.

**Training schedules.** We follow a unified training protocol across benchmarks. For stochastic operator-learning tasks, we train all methods for 100 epochs. For autoregressive rollout benchmarks, we train for 500 epochs. Additional dataset-specific settings (e.g., batch sizes and memory-saving chunking) follow the released configuration files.

### B.3. Dataset Generation Details

This section summarizes the numerical solvers and key hyperparameters used to generate the stochastic operator-learning datasets and the deterministic rollout datasets.

**Stochastic Burgers' equation.** We generate data from the 1D viscous stochastic Burgers' equation on the periodic domain  $x \in [0, 2\pi]$ ,

$$du = \left( -\frac{1}{2} \partial_x(u^2) + \nu \partial_{xx}u \right) dt + \sum_{j=1}^3 \sigma_j \cos(jx) dW_t^j,$$

with viscosity  $\nu = 0.1$  and independent Brownian motions  $\{W_t^j\}_{j=1}^3$ . We discretize space by a pseudo-spectral Fourier method on  $N = 256$  grid points on  $[0, 2\pi]$  with 2/3 de-aliasing. Time integration uses ETDRK4 for the deterministic drift and Euler–Maruyama for the additive noise. We generate one-step pairs with macro step  $\Delta t = 1.0$  using an internal step size  $\Delta t_{\text{sim}} = 10^{-4}$ . The noise is supported on modes  $j \in \{1, 2, 3\}$  with amplitudes  $\sigma_j = \sigma w_j$ , where  $\sigma = 1.0$  and  $(w_1, w_2, w_3) = (1.0, 0.5, 0.1)$ . Initial conditions are sampled as smooth random Fourier series with spectral decay proportional to  $k^{-2}$  (amplitude  $u_{0,\text{amp}} = 1.0$ ). We use 10,000 training inputs and 32 validation/test inputs, with 64 output realizations per input for validation and test.

**Stochastic Darcy flow.** We consider Darcy flow on  $\Omega = (0, 1)^2$ ,

$$-\nabla \cdot (a(x) \nabla u(x)) = f(x), \quad x \in \Omega,$$

where  $a(x)$  is the permeability and  $u(x)$  is the pressure. We discretize  $\Omega$  on a  $128 \times 128$  uniform grid and impose homogeneous Dirichlet boundary conditions. The resulting symmetric positive-definite linear system is solved by a batched conjugate-gradient method (tolerance  $10^{-6}$ , max iterations 5000). The permeability field is sampled as a thresholded Gaussian random field in a DCT-II basis, yielding a binary field  $a(x) \in \{12, 3\}$ . Randomness enters through a mixture source term

$$f(x) = \lambda \sigma_{\text{ln}} \exp(G_{\text{ln}}(x)) + (1 - \lambda) \sigma_{\text{gp}} G_{\text{gp}}(x),$$

where  $G_{\text{ln}}$  and  $G_{\text{gp}}$  are mean-zero Gaussian random fields with RBF-type covariances. In our experiments, we set  $\lambda = 0.1$  and use the scaling parameters  $(\sigma_{\text{ln}}, \ell_{\text{ln}}) = (10.0, 0.2)$  and  $(\sigma_{\text{gp}}, \ell_{\text{gp}}) = (10.0, 0.5)$ , with a small jitter  $10^{-5}$  for numerical stability. Dataset sizes match SBurgers: 10,000 training inputs and 32 validation/test inputs, with 64 output realizations per input for validation and test.

**KS Equation.** We follow the KS scenario from APEBench (Koehler et al., 2024) on a periodic domain of length  $L = 60$  and discretize  $u(\cdot, t) \in \mathbb{R}^{256}$  on a uniform grid. Trajectories are generated with a pseudo-spectral exponential time-differencing scheme (ETDRK, order 2) with 2/3 de-aliasing. We use output spacing  $\Delta t = 1.0$  with 100 internal substeps (i.e.,  $\Delta t_{\text{sim}} = 0.01$ ). We generate 1024 training trajectories of horizon 50 and 128 test trajectories of horizon 100, each preceded by 100 warmup steps. Validation and test splits are obtained by shuffling the test trajectories and splitting them evenly.

**Kolmogorov flow.** We follow the Kolmogorov flow scenario from APEBench (Koehler et al., 2024), based on the 2D incompressible Navier–Stokes equations in vorticity form on  $\Omega = (0, 2\pi)^2$ . We discretize  $\omega(\cdot, t)$  on a  $128 \times 128$  grid and generate trajectories using a pseudo-spectral ETDRK2 integrator with 2/3 de-aliasing under single-mode Kolmogorov forcing. We use output spacing  $\Delta t = 0.25$  with 25 internal substeps (i.e.,  $\Delta t_{\text{sim}} = 0.01$ ). We set  $\nu = 10^{-2}$  and linear drag 0.1 (with the sign convention of APEBench). We generate 256 training trajectories of horizon 50 and 32 test trajectories of horizon 100, each preceded by 400 warmup steps, and form validation and test splits by shuffling and splitting the test set evenly.

## B.4. Metrics

We report complementary accuracy and distributional metrics for stochastic operator learning, and long-horizon forecast metrics for autoregressive rollouts. Throughout, fields are flattened to vectors when computing distances, and all metrics are averaged over conditioning inputs (and over time steps for rollouts). For probabilistic models, we generate an ensemble of  $K$  samples and use the ensemble mean as the point prediction when a deterministic forecast is required.

**Stochastic operator learning.** For each conditioning input, let  $\{x_k\}_{k=1}^K$  denote predicted samples and  $\{y_s\}_{s=1}^S$  denote ground-truth samples. We evaluate distributional agreement using:

- **Energy distance (ED).** We measure the discrepancy between the predictive distribution  $X$  and the data distribution  $Y$  via the energy distance

$$\text{ED}(X, Y) = 2 \mathbb{E}\|X - Y\|_2 - \mathbb{E}\|X - X'\|_2 - \mathbb{E}\|Y - Y'\|_2,$$

where  $X, X'$  are i.i.d. draws from the predictive distribution and  $Y, Y'$  are i.i.d. draws from the empirical data distribution. In practice, expectations are approximated by empirical averages over  $\{x_k\}$  and  $\{y_s\}$ .

- **Sliced Wasserstein distance (SWD).** We report a sliced Wasserstein-1 discrepancy computed by averaging 1D Wasserstein distances over random projection directions  $\{v_p\}_{p=1}^P$ :

$$\text{SWD}(X, Y) = \frac{1}{P} \sum_{p=1}^P W_1(\langle X, v_p \rangle, \langle Y, v_p \rangle).$$

This provides a computationally efficient proxy for Wasserstein-type distributional alignment in high dimensions.

- **NRMSE<sub>m</sub> (mean error).** Let  $\mu_{\text{pred}} = \frac{1}{K} \sum_{k=1}^K x_k$  and  $\mu_{\text{true}} = \frac{1}{S} \sum_{s=1}^S y_s$  denote ensemble means. We report the normalized RMSE

$$\text{NRMSE}_m = \frac{\text{RMSE}(\mu_{\text{pred}}, \mu_{\text{true}})}{\sqrt{\mathbb{E}[\mu_{\text{true}}^2]}}.$$

- **NRMSE<sub>s</sub> (spread error).** Let  $\sigma_{\text{pred}}$  and  $\sigma_{\text{true}}$  denote the pointwise ensemble standard deviations computed from  $\{x_k\}$  and  $\{y_s\}$ , respectively. We report

$$\text{NRMSE}_s = \frac{\text{RMSE}(\sigma_{\text{pred}}, \sigma_{\text{true}})}{\sqrt{\mathbb{E}[\sigma_{\text{true}}^2]}}.$$

**Autoregressive rollouts.** For rollout benchmarks, metrics are computed at each rollout step and then averaged over time (typically excluding the initial condition). For probabilistic models, the point prediction is taken as the ensemble mean  $\mathbb{E}[X]$ .

- **NRMSE.** At each step, we compute RMSE between the point prediction and the ground truth, normalized by the target RMS- $L^2$  at that step, and then average over time.
- **Continuous ranked probability score (CRPS).** We report the empirical CRPS for ensemble forecasts,

$$\text{CRPS} = \mathbb{E}|X - y| - \frac{1}{2} \mathbb{E}|X - X'|,$$

where  $y$  is the ground-truth realization and expectations are approximated using the predicted ensemble.

- **Spread-to-skill ratio (SSR).** To assess calibration under rollout, we report the spread-to-skill ratio

$$\text{SSR} = \frac{\text{spread}}{\text{rmse} + \varepsilon}, \quad \text{spread} = \sqrt{\mathbb{E}[\text{Var}(X)]}, \quad \text{rmse} = \sqrt{\mathbb{E}[(\mathbb{E}[X] - y)^2]},$$

where  $\varepsilon > 0$  is a small constant for numerical stability. Values near 1 indicate that predictive spread is commensurate with forecast error.

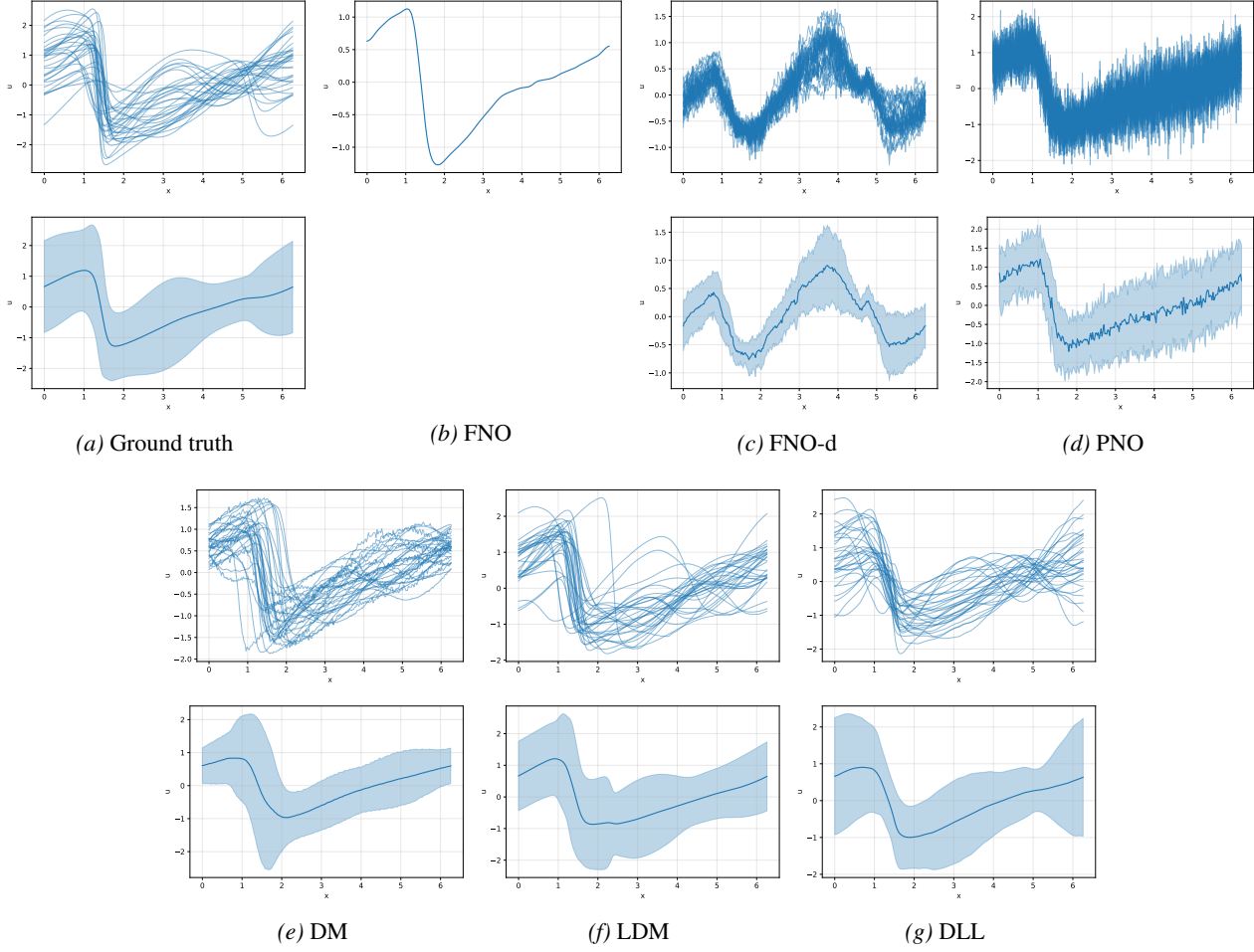


Figure 3. Stochastic Burgers’ equation. Columns compare the ground truth and different surrogate models. For each method, the top panel shows multiple realizations of the solution field  $u(x)$  for a fixed input, illustrating sample diversity. The bottom panel shows the predictive mean (solid line) and an uncertainty band given by standard deviation (shaded region) estimated from the samples.

## C. Qualitative Results

In this section, we visualize conditional samples of the target field generated by our model across our experimental benchmarks.

### C.1. Stochastic Problems

Figure 3 qualitatively compares conditional predictions on the stochastic Burgers’ equation. The ground-truth column exhibits substantial sample-to-sample variability, which is also reflected in the nontrivial standard-deviation band. In contrast, the FNO family produces predictions that are either nearly deterministic or exhibit weakly structured dispersion: although the mean trend can be reasonable, the sampled trajectories concentrate around it and the resulting uncertainty bands are largely uninformative, indicating a failure to capture the conditional spread of the target distribution. Probabilistic baselines such as diffusion in pixel space and its latent variants generate diverse samples, but their variability is less consistently aligned with the ground-truth heteroscedastic structure. Our DLL, by operating in an operator-encoder coefficient space, produces samples whose fluctuations follow the correct spatial dependence and yields uncertainty bands that closely match the ground truth, demonstrating substantially improved modeling of meaningful predictive spread.

Figure 4 presents a qualitative comparison on the stochastic Darcy flow benchmark, reporting the predictive mean (top row) and the predictive standard deviation (bottom row) for a representative test case. The ground truth exhibits spatially structured variability, indicating that uncertainty is strongly heterogeneous across the domain. In contrast, the FNO-based approaches,

including deterministic FNO, dropout-augmented FNO, and PNO, do not recover a meaningful uncertainty structure. In our experiments these baselines also tend to overfit, and model selection based on the best validation checkpoint often returns early, non-converged states whose mean and variance maps are qualitatively inconsistent with the target statistics. By comparison, DLL produces both a mean field that matches the large-scale solution structure and a standard-deviation map that aligns with the ground-truth spatial pattern. This indicates that DLL successfully learns distributional information through explicit conditional generative modeling in the operator-encoder coefficient space, rather than relying on implicit or weak stochasticity in the backbone.

## C.2. Autoregressive Rollouts

Figure 5 compares long-horizon rollout predictions for the KS system at the 50th step, overlaying the ground truth (black) with each method’s predictive mean (blue) and a standard deviation band computed from generated samples (shaded). While FNO and PNO remain reasonably accurate in terms of the mean trajectory, their uncertainty bands are systematically too narrow relative to the observed mismatch to the ground truth, indicating overconfident uncertainty estimates under chaotic error amplification. Diffusion-based baselines yield wider spreads but may sacrifice mean fidelity. In contrast, DLL preserves competitive accuracy while producing a visibly more informative spread around the mean, better reflecting rollout uncertainty and providing more credible uncertainty quantification in this long-horizon regime.

Figure 6 reports qualitative rollout results for Kolmogorov flow at the 50th prediction step, showing the predictive mean (top), predictive standard deviation (middle), and the pointwise error for the same test case (bottom). A key observation is that diffusion-based generative surrogates produce uncertainty maps that meaningfully track where the rollout is difficult: regions with larger pointwise error tend to coincide with elevated predictive standard deviation. This correlation is visible for both pixel-space and latent diffusion baselines and is especially clear for DLL, whose uncertainty highlights the same coherent structures that dominate the error field while maintaining a competitive mean prediction. In contrast, non-generative baselines often yield weakly structured or poorly aligned uncertainty patterns, suggesting that explicit generative modeling is important for producing uncertainty estimates that reflect rollout error under long-horizon dynamics.

Figure 7 summarizes long-horizon rollout performance on KS (top) and Kolmogorov flow (bottom) using complementary accuracy and uncertainty metrics. NRMSE (left) and CRPS (middle) generally increase with rollout step, reflecting error accumulation and growing distributional mismatch in chaotic dynamics.

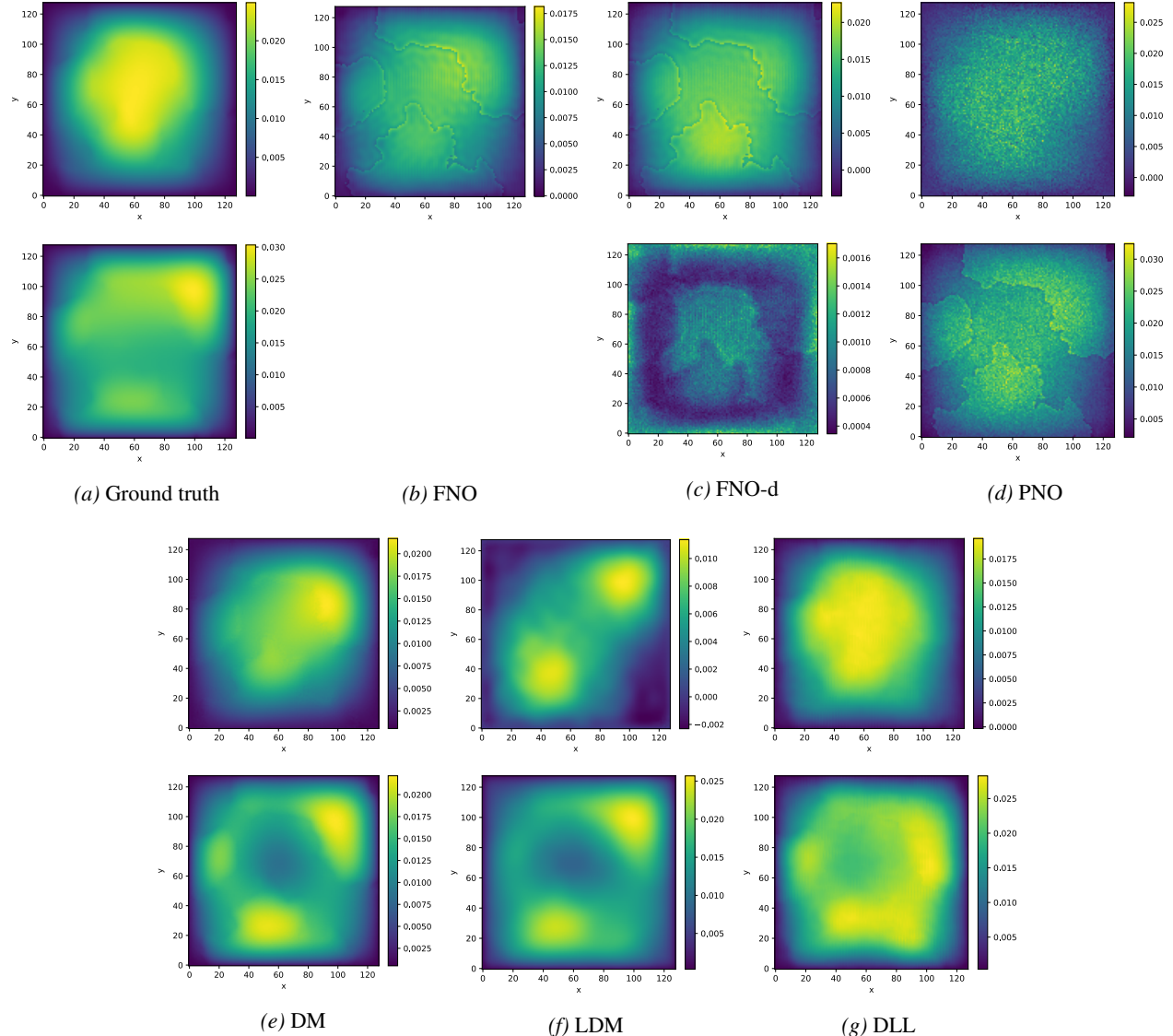


Figure 4. Stochastic Darcy flow. For each method, we generate conditional samples of the solution field and summarize them by the sample mean (top) and per-pixel sample standard deviation (bottom). This visualization highlights both accuracy of the central prediction and the spatial structure of predictive uncertainty.

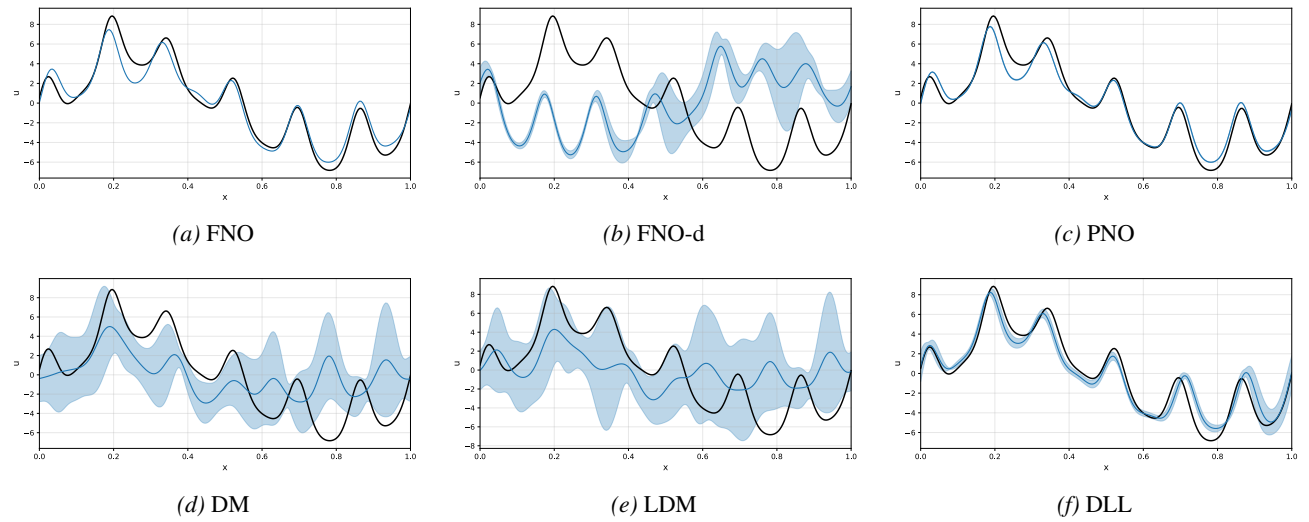


Figure 5. KS equation. Long-horizon rollout comparison at rollout step 50. The black curve denotes the ground-truth solution, while the blue curve shows the predictive mean of each method. Shaded regions indicate predictive standard deviation estimated from generated samples.

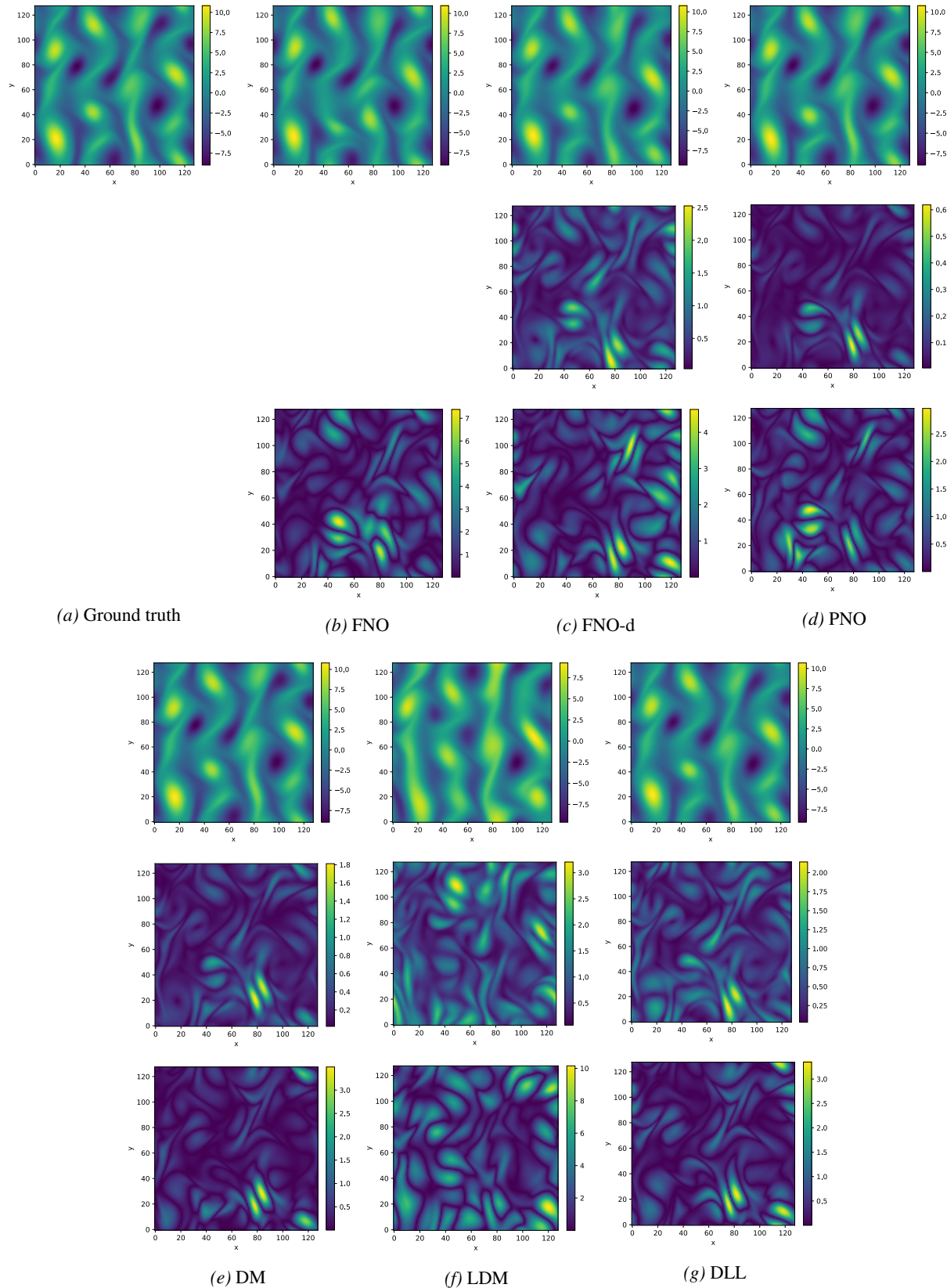


Figure 6. Kolmogorov flow. Rollout evaluation at the 50th step. Rows show the predictive mean (top), predictive standard deviation (middle), and the pointwise absolute error (bottom) for a representative test case across baselines and DLL.

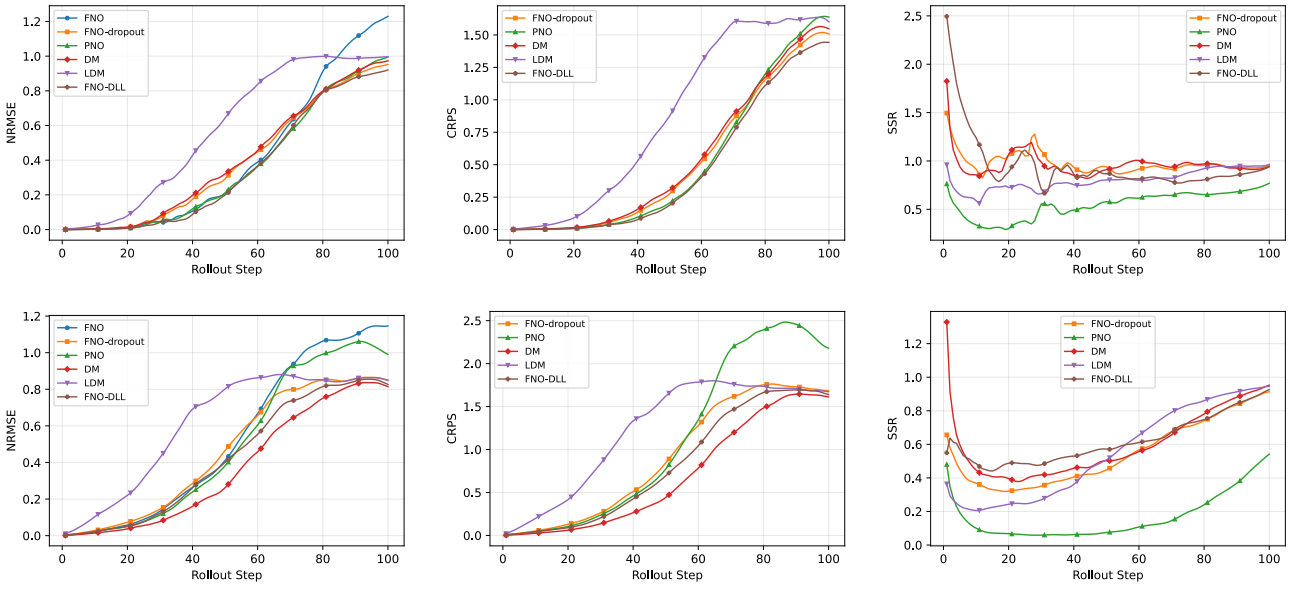


Figure 7. Rollout evaluation on KS (top row) and Kolmogorov flow (bottom row). We report NRMSE (left), CRPS (middle), and SSR (right) as a function of rollout step for baselines and DLL, illustrating long-horizon accuracy and uncertainty calibration.